

This is an electronic reprint of the original article. This reprint may differ from the original in pagination and typographic detail.

Sizing and packing of particles – Characterization of mono-, di- and trimodal particle assemblies

Rosenholm, Jarl B.

Published in:
Advances in Colloid and Interface Science

DOI:
[10.1016/j.cis.2023.102887](https://doi.org/10.1016/j.cis.2023.102887)

Published: 01/05/2023

Document Version
Final published version

Document License
CC BY

[Link to publication](#)

Please cite the original version:
Rosenholm, J. B. (2023). Sizing and packing of particles – Characterization of mono-, di- and trimodal particle assemblies. *Advances in Colloid and Interface Science*, 315, Article 102887.
<https://doi.org/10.1016/j.cis.2023.102887>

General rights

Copyright and moral rights for the publications made accessible in the public portal are retained by the authors and/or other copyright owners and it is a condition of accessing publications that users recognise and abide by the legal requirements associated with these rights.

Take down policy

If you believe that this document breaches copyright please contact us providing details, and we will remove access to the work immediately and investigate your claim.



Historical Perspective

Sizing and packing of particles – Characterization of mono-, di- and trimodal particle assemblies

Jarl B. Rosenholm*

Physical Chemistry, Laboratory of Molecular Science and Engineering, Aurum, Åbo Akademi University, Henriksgatan 2, 20500 Åbo (Turku), Finland

ARTICLE INFO

Keywords:

Particle size and shape
 Particle size classes from distribution
 Mono-, di- and trimodal particle packing
 Dependence on test compartment
 Fractal dimensions
 Cluster energy

ABSTRACT

The influence of particle size and shape on the properties of mono-, di- and trimodal particle assemblies is evaluated. The relative increase of surface area over bulk when particle size is reduced renders particles in the colloid (10–100 nm) and nano (1–10 nm) ranges extraordinary properties. Asymmetric particle shapes are characterized by sphericity and represented by equivalent spheres. The average diameter of particle size classes (size ranges) of powders are dependent on two experimentally determined properties. Average particle sizes (median, mean and mode) for each size class are extracted from size distributions of powders. Mono-, di- and trimodal particle packing efficiency is expressed as volume fractions and inverted volume fractions of close-packed hard spheres and related to standard cubic, orthorhombic, tetragonal-sphenoidal and rhombohedral-hexagonal packing properties. Simple models are presented to reveal the relative influence of fine, medium, and coarse particles and their ratios on powder properties. Experimental challenges relate to the influence of test compartment size and shape on particle layering and of particle shape on packing density. Particle asymmetry induces preferential aggregation through bond and site percolation resulting in dense closed or loose open cluster structures relating to particle segregation. Clusters may be characterized by structural fractals while textural fractals identify the particles involved. A modified Flory-Huggins lattice model for macromolecular solutions enables determination of combinatory entropy for cluster formation. A model is presented which relates time dependent volume fraction to logarithmic time dependence of compaction. This review concerns mixing of dry particles which corresponds to molecular processes at the gaseous (continuum, vacuum) reference state.

1. Introduction

Recently, enhanced interest has been focused on the extraordinary properties of particles in μm (10^{-6} m) – nm (10^{-9} m) size range. In early 1900 the first sets of nearly monodispersed nanometer sized sols were prepared (Zsigmondy, von Weymarn, etc.) with an average radius in nanometer range. Numerous Nobel prizes were since awarded in physics and in chemistry to surface- and colloid researchers [1]. In 1959 Feynman drew attention of physics community to the vast technological opportunities of fine particles [2]. This led to the foundation of nano size particle technology and later much of surface and colloid science was “reinvented” as nanoscience. Therefore, a particular attention is paid to the properties of fine particles alone and of mixed with coarse particles. Models for packing of mono- and multimodal particles are based on hard spheres. It was deemed necessary to shortly review the properties of particle size ranges (classes) as well as the influence of asymmetry in terms of three-dimensional sphericity and projected two-dimensional

circularity on packing efficiency. Particle size classes are extracted from size distribution (median, mean and mode) of powders and the average size of each size range (particle class) is characterized by two experimentally available properties.

A proper definition of particle size and shape enables an analysis of packing mono-, bi- and tri-modal particle powders with reference to standard cubic, orthorhombic, tetragonal-sphenoidal and rhombohedral-hexagonal closepacking of hard spheres. The rather confusing procedures applied within “particle community” are replaced by straightforward representation of particle packing in terms of volume fractions. The obscure dimensionless “apparent volume” is replaced by proper inverse volume fraction. Simple models to reveal the relative influence of amount and size of particles are presented and evaluated. The influence of each particle size on powder compaction is exhibited and quantified.

Challenges related to experimental conditions are discussed. Such factors are enhanced particle layering at extended walls creating

* Corresponding author.

E-mail address: jarl.rosenholm@abo.fi.<https://doi.org/10.1016/j.cis.2023.102887>

Received in revised form 23 March 2023;

Available online 28 March 2023

0001-8686/© 2023 The Author. Published by Elsevier B.V. This is an open access article under the CC BY license (<http://creativecommons.org/licenses/by/4.0/>).

excluded volumes and dependence on number of layers. The dependence on wall curvature reveals a dependence of packing on test container size and shape. The particle asymmetry has a strong influence on powder compaction. Asymmetric particles form “bonds” at the edges which results in bond and site percolation to macroscopic particle gels. Models have been designed to evaluate probabilities for closed and open cluster structures. Open structures allow small particles to segregate from the gel (cluster) matrix. Fractal dimension analysis enables characterization of one-, two- and three-dimensional structural fractals and textural fractals which represent macroscopic clusters and particles being a part of the network. Flory-Huggins lattice model modified to apply for dry particle systems enables calculation of a combinatory entropy for the cluster networks. A model is presented which relates time dependent volume fraction to logarithmic time dependence of compaction.

Mixing of dry particles corresponds to molecular processes at gaseous (continuum, vacuum) reference state. Since wet conditions, including particle synthesis and dissolution involve additional strong interactions such systems are excluded from this review.

2. Characterization of particles

Little attention is usually paid on the detailed nature of particles. They are generally considered (nearly) spherical and of almost equal size (monodisperse). It is therefore necessary to recall the real properties of single particles and particle size fractions. Particularly interesting is to reveal why particle powders change from extremely cohesive to dry fluids (dust) as the particle size is reduced. Moreover, it seems necessary to introduce proper definitions of micro-, colloid- and nanoparticles.

2.1. Classification of particle sizes

Particle sizes are reported as average diameters of equivalent spheres. When the composition of molecular particles is known the molecular (monomer, v_1) volume and size is readily computed as:

$$v_1 = \frac{M_1}{\rho_1 N_A} = \frac{\pi}{6} d_v^3 = k_v d_v^3 \Leftrightarrow d_v = 2r_v = 2\sqrt[3]{\frac{3v_1}{4\pi}} \quad (1)$$

where k_v = shape coefficient, M = molar mass (molecular weight), ρ = density and N_A = Avogadro’s number. The average monomer equivalent surface area is available as:

$$a_1 = 4\pi r_v^2 = \pi d_a^2 \Leftrightarrow d_a = \sqrt{\frac{a_1}{\pi}} \quad (2a)$$

The corresponding area per unit volume is defined as:

$$a_v = \frac{a_1}{v_1} = \frac{6d_a^2}{d_v^3} \quad (2b)$$

The projected (two-dimensional) area is:

$$a_{2D} = \pi r_{2D}^2 = \frac{\pi}{4} d_{2D}^2 = k_{2D} d_{2D}^2 \Leftrightarrow d_{2D} = \sqrt{\frac{4a_{2D}}{\pi}} \quad (3)$$

where k_{2D} = shape coefficient. When averaged over all possible orientations $d_{2D} = d_a$ for convex particles. The perimeter (p_{2D} , circular length) of the corresponding projected circle having same a_{2D} is:

$$p_{2D} = 2\pi r_{2D} = \pi d_{2D} = k_{2D} d_{2D} \quad (4)$$

The equivalent size, area and volume of some typical liquid, polymer and mineral samples are listed in Table 1.

The size properties listed in Table 1 are based on the monomer diameter defined in Eq. (1). The monomer Gibbs free energy $g_1 = \Delta f_0 G_m / N_A$ aJ (aJ = 10^{-18} J, $\Delta f_0 G_m$ = molar Gibbs formation energy) and the dispersive (D) surface tension/energy has been calculated as $\sigma_S^D = 4.87 \cdot 10^{20} H_{SS} \text{ mJ/m}^2$ (H_{SS} = Hamaker constant) [6]. As shown by water, the dispersive surface tension is only a part of the experimental (total) surface tension/energy.

Considering available experimental methods, volumes (gravimetry), areas (gas adsorption) and perimeters (microscopy) of particles ($V_p = N_p v_1$, $A_p = N_p a_1$, N_p = number of monomers in particle) can be experimentally determined and individual property dependent non-equal sizes calculated using Eqs. (1) to (4). Molecules in the surface layer possess extra ordinary electronic properties (surface states) due to broken bonds which result in extended distances from equilibrium position. The total energy of a unit volume is the sum of Gibbs free energy of the bulk particle and its surface energy:

$$G_p = C_p^b + C_p^s = G_p^b + A_p \sigma_s \quad (5)$$

The contribution of abnormal surface electronic and catalytic properties is enhanced when particle size is reduced. To illustrate the relative contributions of bulk energy and energy of the surface layer we choose a cube with 1 mm side length ($V_p = 1 \text{ mm}^3 = 10^{-9} \text{ m}^3$, $A_p = 6 \text{ mm}^2 = 6 \cdot 10^{-6} \text{ m}^2$). This cube is divided into an increasing number (N_c) of smaller cubes maintaining the initial total volume (V_p) constant. The surface layer is chosen to be 1 nm thick, which according to Table 1 encompass one-to-three molecular layers. Alternatively, the surface layer could be chosen as a monomolecular layer, but then the thickness would vary for each substance. The overall Gibbs (free) energy of each cube volume is written as:

Table 1

Monomer molar mass (M_1 /(g/mol)), density (ρ_1 /(g/cm³)), diameter (d_1 /nm), area (a_1 /nm²), projected area (a_{2D} /nm²), perimeter length (p_{2D} /nm), and volume (v_1 /nm³) of some typical liquid monomers, polymers, and mineral molecules; *n*-C₆ = hexane, *n*-C₁₆ = hexadecane, *PS* = polystyrene, *PVC* = polyvinylchloride, *PTFE* = Teflon. Gibbs free energy of formation of molecules (–g/aJ, aJ = 10^{-18} J), calculated and experimental dispersive surface tension/energy (σ_S^D /(mJ/m²)) [3–5].

	M_1 g/mol	ρ_1 g/cm ³	v_1 nm ³	d_1 nm	a_1 nm ²	a_{2D} nm ²	p_{2D} nm	–g ₁ aJ	σ_S^D mJ/m ²	σ_S^{exp} mJ/m ²
H ₂ O	18.015	0.997	0.0300	0.385	0.467	0.117	0.606	0.394	18.02	72.8
n-C ₆	114.23	0.703	0.2698	0.802	2.019	0.505	1.259	0.011	21.92	21.6
n-C ₁₆	226.41	0.770	0.4882	0.977	2.998	0.750	1.535	0.018	25.32	27.5
PS	104.10	1.04	0.1662	0.682	1.462	0.365	1.071	0.007	32.14	33.0
PVC	62.50	1.38	0.0752	0.524	0.862	0.215	0.823		37.99	39.0
PTFE	100.02	2.20	0.0755	0.524	0.864	0.216	0.824		18.51	18.3
SiO ₂	60.08	2.65	0.0376	0.416	0.543	0.136	0.653	1.422	31.90	
CaCO ₃	100.09	2.71	0.0613	0.489	0.752	0.188	0.768	1.874	49.19	
CaF ₂	78.075	3.18	0.0408	0.427	0.573	0.143	0.671	1.938	35.06	
SiC	40.11	3.21	0.0207	0.341	0.365	0.091	0.535		214.3	
Al ₂ O ₃	101.96	3.95	0.0429	0.434	0.592	0.148	0.682	2.627	68.18	
TiO ₂	79.87	4.23	0.0313	0.391	0.481	0.120	0.614		209.4	
Fe ₂ O ₃	159.69	5.24	0.0506	0.459	0.662	0.165	0.721	1.232		
Fe ₃ O ₄	231.53	5.17	0.0744	0.522	0.855	0.214	0.819	1.686	102.3	
ZrO ₂	123.22	5.68	0.0360	0.410	0.527	0.132	0.644		131.5	

$$g_N = \frac{G_p}{N_c} = \frac{N_p g_1}{N_c} \Leftrightarrow g_v = \frac{g_N}{v_N} = \frac{g_N^b}{v_N^b} + \frac{g_N^s}{v_N^s} = g_v^b + \frac{a_N}{v_N^s} \sigma_s \quad (6)$$

where the surface volume of each cube is $v_N^s = v_N - v_N^b$. The volume of each cube is related to equivalent spheres ($d_N = 2r_N$) as:

$$l_N^3 = v_N = \frac{\pi}{6} d_N^3 \Leftrightarrow l_N^3 = 0.5236 d_N^3 \quad (7a)$$

$$(l_N^b)^3 = (l_N - 2nm)^3 = v_N^b = \frac{\pi}{6} (d_N^b)^3 \Leftrightarrow (l_N^b)^3 = 0.5236 (d_N^b)^3 \quad (7b)$$

The relationship between the area of each cube and the area of corresponding sphere is:

$$6l_N^2 = a_N = \pi d_N^2 \Leftrightarrow l_N^2 = 0.5236 d_N^2 \quad (8)$$

The initial volume remains constant $V_p = N_c v_N = (1 \text{ mm})^3 = 10^{-9} \text{ m}^3$ but the surface area increases $A_p = N_c a_N$ (Fig. 1). Therefore, the total area per constant volume, $A_p/V_p = a_N/v_N = N_1 a_1 / N_1 v_1 = a_1/v_1$ increases.

The general properties of particles in mm (10^{-3} m) to nm (10^{-9} m) size range are listed in Table 2. The area-to-volume ratio and the per cent surface volume serves as a measure of exceptional colloid and/or nano properties.

As shown by $A_p/V_p = a_N/v_N = a_1/v_1$ ratio and by per cent surface volume (v_1^s) the contribution of surface energy (Eq. (6)) is increasing as compared to bulk energy when particle sizes decreases. This is particularly apparent in the 100 nm – 1 nm range. In the nano-size range (1–10 nm) the surface volume ($N_c v_N^s$) exceeds the bulk volume ($N_c v_N^b$).

2.2. Classification of particle shapes

Particles are seldom spheres or cubes but have irregular shapes. When investigating them a common practice is to lay particles on their widest (most stable) surface. Heywood characterized (irregular) particles based on mutually perpendicular maximum length (l), maximum width (w) and maximum height (h) [7,8]. He assumed that $l < w < h$. Cubes are then characterized by $l = w = h$, platelets by $l = w \gg h$ and needles by $l \gg w = h$. In general flatness ratio was expressed as (w/h) and as elongation ratio as (l/w). The particle volume and surface area can be expressed in terms of these parameters as:

$$V_p = k_v d_v^3 = l \cdot w \cdot h \quad (9a)$$

$$A_p = k_a d_a^2 = 2(l \cdot w + w \cdot h + l \cdot h) \quad (9b)$$

Based on Heywood parameters particles can be identified as (spheric, cubic, tetrahedral) geometric shape groups and as non-geometrical (rounded, sub-angular, prismatic angular, tetrahedral angular) shape groups.

Feret and Martin have classified irregular particles and developed methods to extract equivalent spherical diameters for them (Fig. 2) [9]. Feret's diameter is defined as the mean value between pairs of parallel

tangents to projected outline of particles. Martin's diameter is the mean chord length of projected outline of particles which divides the particle projection area in two equal parts. When the volume, surface area and projected area or perimeter length are experimentally determined, Eqs. (1) to (4) may be used to establish an equivalent sphere or circle of irregular particles. The size of these circles is obviously very dependent on the used experimental method.

Viewed from the top, packing of layered mono-sized equivalent spheres may be characterized either by triangles or squares. The angle between adjoining spheres is $\pi/3$ or $\pi/2$, respectively. Increasing the number of spheres in the layers the triangles expand to a hexagonal pattern and the squares to a symmetrical grid (Fig. 3).

Only four three-dimensional arrangements are possible for close-packed monomodal equivalent spheres; cubic, orthorhombic, tetragonal and rhombohedral. Fig. 4 illustrates the triangular pyramid and cuboid unit cells connecting the centers of these spheres.

Cubic packing has three equal perpendicular unit cell side lengths, orthorhombic packing has two equal and one unequal perpendicular unit cell side lengths, tetragonal and rhombohedral packing has three unequal perpendicular unit cell side lengths and rhombohedral (triangular) packing have two tilted equal perpendicular unit cell side lengths. The unit cell dimensions are listed in Table 3.

The volumes may be calculated according to Heywood's procedure (Eq. (9a)) and relate the volumes to equivalent spherical arrangements through their radii (see later).

Based on equivalent spheres, Wadell's (true) sphericity index is defined as the ratio of the surface area of a sphere having the same volume as the particle to its actual area (A_p) [10,11]:

$$\psi = \frac{A_v}{A_p} \approx \left(\frac{d_v}{d_A} \right)^2 \Leftrightarrow \psi = \frac{\sqrt[3]{36\pi V_p^2}}{A_p} \quad (10a)$$

Assuming that the asymmetric particle may be represented by an equivalent ellipsoid the sphericity index may be expressed [12] as:

$$\psi = \sqrt[3]{\frac{d_s^3}{d_l d_m}} \Leftrightarrow e_{xy} = \frac{d_m}{d_l}, e_{xz} = \frac{d_s}{d_l}, e_{yz} = \frac{d_s}{d_m} \quad (10b)$$

where the elongations (e) may be expressed by the shortest (d_s), medium (d_m) and longest (d_l) particle diameters. Table 4 relates sphericity to some symmetric angular objects.

Note that tetra- to icosahedrons have, opposite to the triangular pyramid and cuboid objects listed in Table 3, an increasing number of symmetric side planes. Tetrahedrons have four equal side planes of length l . Their width (w) is, $(3)^{1/2}l/2$ and their height (h) is, $2(2)^{1/2}w/3 = (2)^{1/2}l/2$, which results in the volume and surface area given in Table 4.

The two-dimensional outline of a sphere, a circle, is defined (Eqs. (3), (4)) by Sneed's circularity [9,12,13]:

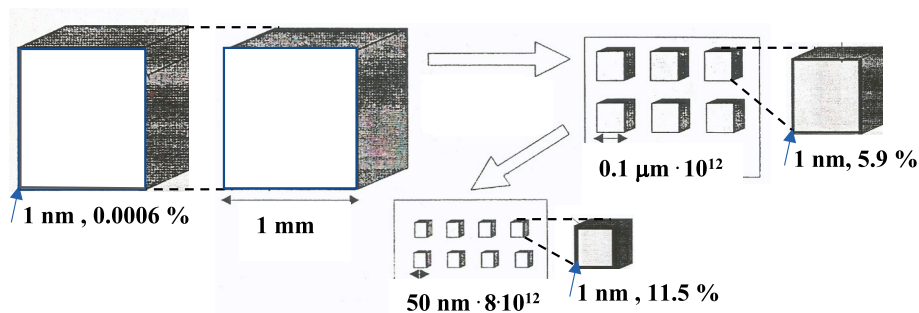


Fig. 1. Division of a 1 mm^3 cube into a growing number of smaller cubes keeping the total volume constant. A 1 nm thick surface layer increases the fraction (percentage) of surface volume.

Table 2

Side length (diameter, l_N) of cubic unit particles, their unit volume ($N_c v_N$), number of cubes (N_c), unit area ($N_c a_N$), area-to-volume ratio (a_N/v_N), reduced bulk unit volume ($v_N^b = v_N - v_N^s$) and per cent units in surface layer v_N^s (%).

l_N	l_N m	v_N m ³	N_c	a_N m ²	a_N/v_N	v_N^b m ³	v_N^s m ³	v_N^s %
1 mm	1·10 ⁻³	1·10 ⁻⁹	1	6·10 ⁻⁶	6·10 ³	1·10 ⁻⁹	6·10 ⁻¹⁵	6·10 ⁻⁴
100 μm	1·10 ⁻⁴	1·10 ⁻¹²	1·10 ³	6·10 ⁻⁸	6·10 ⁴	1·10 ⁻¹²	6·10 ⁻¹⁷	6·10 ⁻³
10 μm	1·10 ⁻⁵	1·10 ⁻¹⁵	1·10 ⁶	6·10 ⁻¹⁰	6·10 ⁵	1·10 ⁻¹⁵	6·10 ⁻¹⁹	6·10 ⁻²
1 μm	1·10 ⁻⁶	1·10 ⁻¹⁸	1·10 ⁹	6·10 ⁻¹²	6·10 ⁶	1·10 ⁻¹⁸	5.99·10 ⁻²¹	0.6
100 nm	1·10 ⁻⁷	1·10 ⁻²¹	1·10 ¹²	6·10 ⁻¹⁴	6·10 ⁷	9.41·10 ⁻²²	5.88·10 ⁻²³	5.9
90 nm	9·10 ⁻⁸	7.29·10 ⁻²²	1.37·10 ¹²	8.10·10 ⁻¹⁵	1.11·10 ⁷	6.81·10 ⁻²²	4.75·10 ⁻²³	6.5
80 nm	8·10 ⁻⁸	5.12·10 ⁻²²	1.95·10 ¹²	6.40·10 ⁻¹⁵	1.25·10 ⁷	4.75·10 ⁻²²	3.74·10 ⁻²³	7.3
70 nm	7·10 ⁻⁸	3.43·10 ⁻²²	2.92·10 ¹²	4.90·10 ⁻¹⁵	1.43·10 ⁷	3.14·10 ⁻²²	2.86·10 ⁻²³	8.3
60 nm	6·10 ⁻⁸	2.16·10 ⁻²²	4.63·10 ¹²	3.60·10 ⁻¹⁵	1.67·10 ⁷	1.95·10 ⁻²²	2.09·10 ⁻²³	9.7
50 nm	5·10 ⁻⁸	1.25·10 ⁻²²	8.00·10 ¹²	2.50·10 ⁻¹⁵	2.00·10 ⁷	1.11·10 ⁻²²	1.44·10 ⁻²³	11.5
40 nm	4·10 ⁻⁸	6.40·10 ⁻²³	1.56·10 ¹³	1.60·10 ⁻¹⁵	2.50·10 ⁷	5.49·10 ⁻²³	9.13·10 ⁻²⁴	14.3
30 nm	3·10 ⁻⁸	2.70·10 ⁻²³	3.70·10 ¹³	9.00·10 ⁻¹⁶	3.33·10 ⁷	2.19·10 ⁻²³	5.05·10 ⁻²⁴	18.7
20 nm	2·10 ⁻⁸	8.00·10 ⁻²⁴	1.25·10 ¹⁴	4.00·10 ⁻¹⁶	5.00·10 ⁷	5.83·10 ⁻²⁴	2.17·10 ⁻²⁴	27.1
10 nm	1·10 ⁻⁸	1.00·10 ⁻²⁴	1.00·10 ¹⁵	1.00·10 ⁻¹⁶	1.00·10 ⁸	5.12·10 ⁻²⁵	4.88·10 ⁻²⁵	48.8
9 nm	9·10 ⁻⁹	7.29·10 ⁻²⁵	1.37·10 ¹⁵	8.10·10 ⁻¹⁷	1.11·10 ⁸	3.43·10 ⁻²⁵	3.86·10 ⁻²⁵	52.9
8 nm	8·10 ⁻⁹	5.29·10 ⁻²⁵	1.95·10 ¹⁵	6.40·10 ⁻¹⁷	1.25·10 ⁸	2.16·10 ⁻²⁵	3.13·10 ⁻²⁵	59.2
7 nm	7·10 ⁻⁹	3.43·10 ⁻²⁵	2.91·10 ¹⁵	4.90·10 ⁻¹⁷	1.43·10 ⁸	1.25·10 ⁻²⁵	2.18·10 ⁻²⁵	63.6
6 nm	6·10 ⁻⁹	2.16·10 ⁻²⁵	4.63·10 ¹⁵	3.60·10 ⁻¹⁷	1.67·10 ⁸	6.40·10 ⁻²⁶	1.52·10 ⁻²⁵	70.4
5 nm	5·10 ⁻⁹	1.25·10 ⁻²⁵	8.00·10 ¹⁵	2.50·10 ⁻¹⁷	2.00·10 ⁸	2.70·10 ⁻²⁶	9.80·10 ⁻²⁶	78.4
4 nm	4·10 ⁻⁹	6.40·10 ⁻²⁶	1.56·10 ¹⁶	1.60·10 ⁻¹⁷	2.50·10 ⁸	8.00·10 ⁻²⁷	5.60·10 ⁻²⁶	87.5
3 nm	3·10 ⁻⁹	2.70·10 ⁻²⁶	3.70·10 ¹⁶	9.00·10 ⁻¹⁸	3.33·10 ⁸	1.00·10 ⁻²⁷	2.60·10 ⁻²⁶	96.3
2 nm	2·10 ⁻⁹	8.00·10 ⁻²⁷	1.25·10 ¹⁷	4.00·10 ⁻¹⁸	5.00·10 ⁸			
1 nm	1·10 ⁻⁹	1.00·10 ⁻²⁷	1.00·10 ¹⁸	1.00·10 ⁻¹⁸	1.00·10 ⁹			

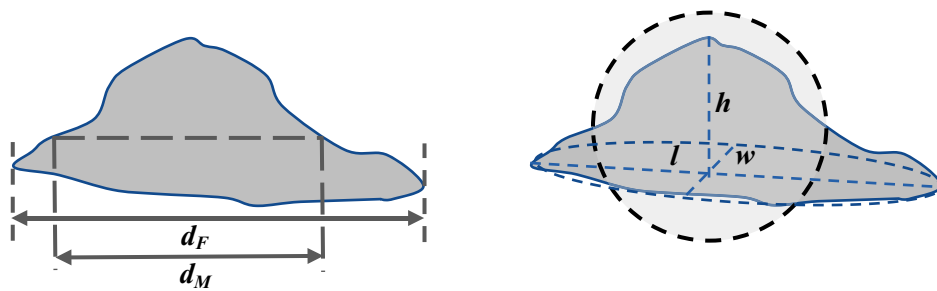


Fig. 2. Schematic side projection of maximum of an irregular particle with base length (l), base width (w), height (h), Feret's diameter (d_F) and corresponding Martin's diameter (d_M). Equivalent circle with equal projected surface area (d_{2D}). Note that at proper projection, $l > w > h$.

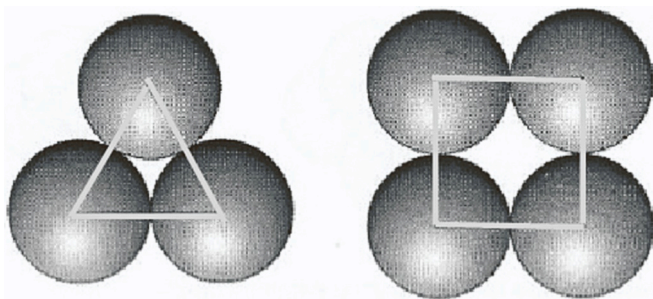


Fig. 3. Layered mono-sized equivalent spheres may be characterized either by triangles or squares.

$$\omega = \frac{P_{2D}^2}{4\pi a_{2D}} \approx \frac{1}{\pi d_{2D}} \quad (11)$$

Circularity may also be expressed as the ratio of the perimeter of a circle having the same area as the projected area of the particle to its actual perimeter. Diameters will vary according to employed sphericity units and type of measurement dependent diameter.

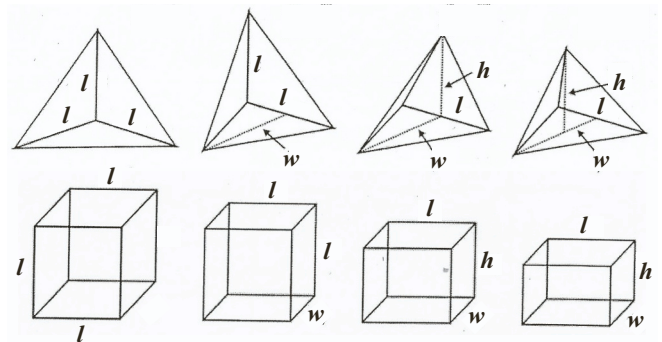


Fig. 4. Schematic illustration of unit cells of monomodal packing formations (side length $l (= 2r = d)$, width w , height h); cubic (first figure from left), orthorhombic (second figure from left), tetragonal (third figure from left) and rhombohedral (figure to right). The length of unmarked sides varies.

2.3. Characterization of particle size classes - powders

In accordance to **Table 2** particles with relative diameters (spheres or cubes) 1:2:3:4:5:6:7:8:9:10 represent ten size classes for which their number ($N = 10$), length (L), volume (V), surface area (A) and moment (M) can be determined. To condense the mathematical expression





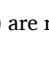
Table 3

Length ($l = 2r = d$), width (w), height (h), coordination number (N_C) and volume (v_C) of pyramidal and cuboid unit cells in terms of radii (r) of close-packed spheres arranged in cubic (Cu), orthorhombic (Or), tetragonal (Te) and rhombohedral (Rh) order.

	Cu	Or	Te	Rh
Coord. nr. N_C	6	8	10	12
Length, l	$2r$	$2r$	$2r$	$2r$
Width, w	$2r$	$(3)^{1/2}r$	$(3)^{1/2}r$	$(3)^{1/2}r$
Height, h	$2r$	$2r$	$(3)^{1/2}r$	$2(6)^{1/2}r/3$
Volume, v_C	$8r^3$	$4(3)^{1/2}r^3$	$6r^3$	$4(2)^{1/2}r^3$

Table 4

Comparison of volume, surface area and sphericity of some reference solid shapes to approximate sphericity of few particles ($l = 2r = d$) side of unit cells): $k_{dh}(V_p) = (15 + 7(5)^{1/2})/4$, $k_{dh}(V_p) = 5(3 + (5)^{1/2})/12$, $k_{dh}(A_p) = (25 + 10(5)^{1/2})^{1/3}$ [12].

Shape	Figure	Vp	Ap	ψ	Example	ψ
Tetrahedron		$(2)^{1/2}l^3/12$	$(3)^{1/2}l^2$	0.671	crushed glass	0.65
Cube (hexah.)		l^3	$6l^2$	0.806	sandstone	0.80-
Octahedron		$(2)^{1/2}l^3/3$	$2(3)^{1/2}l^2$	0.846	norm. salt	0.84
Dodecahedron		$k_{dh}l^3$	$k_{dh}l^2$	0.910	round sand	0.92-
Icosahedron		$k_{dh}l^3$	$5(3)^{1/2}l^2$	0.939	round sand	-0.98

particle sizes (s) are related to diameters in the following way:

Volume:

$$V_p = \frac{\pi}{6}d_V^3 = k_V d_V^3 = s_V^3 \Leftrightarrow dV_p = s_V^3 dN \quad (12a)$$

Surface area:

$$A_p = \pi d_A^2 = k_A d_A^2 = s_A^2 \Leftrightarrow dA_p = s_A^2 dN \quad (12b)$$

where coefficients k express the geometrical shape and N the number of particles. The averages using two of particle class properties are shown in Table 5.

The volume moment mean equals the the mean of a typical size distribution (discussed later). As shown, the average diameter of size classes varies considerably depending on which properties are combined. The overall properties of each size class are illustrated in Fig. 5.

Mineral particles in 0.1–10 mm range can be mechanically produced and possess considerable fluidity due to sufficient mass (gravity) and small interparticle cohesion. In 1–100 μm ranges (microparticles) the increased number of broken lattice surfaces increases attraction (catalytic activity) between crystal planes resulting in enhanced interparticle cohesion. The mechanical processing of such particles become difficult and need space or a polar solvent to reduce attraction. The thermal movement of colloid particles in 10 nm – 1 μm range results in enhanced repulsion and fluidity which overcomes gravitation. In a closed system

Table 5

Mean average sizes (s) of ten particle classes for which diameter of equivalent spheres are 1:2:3:4:5:6: 7:8:9:10 ($N = 10$). Input data, length $L = \sum s dL = 55$, surface area $A = \sum s^2 dN = 385$, volume $V = \sum s^3 dN = 3025$, moment $M = \sum s^4 dN = 25,333$. [9].

Number, length mean	$s_{NL} = \sum dL / \sum dN = \sum s dN / \sum dN$	$s_{NL} = 5.50$
Number, area mean	$s_{NA} = \sqrt{\sum dA / \sum dN} = \sqrt{\sum s^2 dN / \sum dN}$	$s_{NA} = 6.20$
Number, volume mean	$s_{NV} = \sqrt[3]{\sum dV / \sum dN} = \sqrt[3]{\sum s^3 dN / \sum dN}$	$s_{NV} = 6.71$
Length, surface mean	$s_{LA} = \sum dA / \sum dL = \sum s^2 dN / \sum s dN$	$s_{LA} = 7.00$
Length, volume mean	$s_{LV} = \sqrt{\sum dV / \sum dL} = \sqrt{\sum s^3 dN / \sum s dN}$	$s_{LV} = 7.42$
Surface, volume mean	$s_{AV} = \sum dV / \sum dA = \sum s^3 dN / \sum s^2 dN$	$s_{AV} = 7.86$
Volume, moment mean	$s_{VM} = \sum dM / \sum dV = \sum s^4 dN / \sum s^3 dN$	$s_{VM} = 8.37$

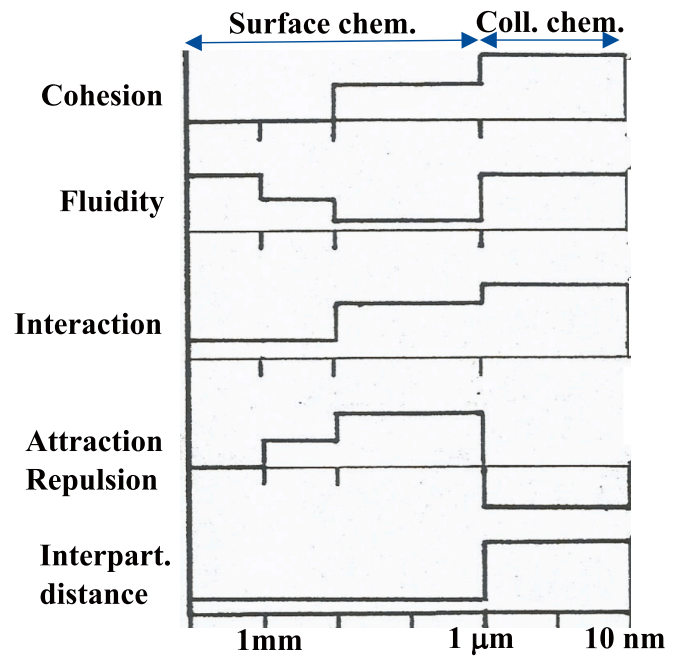


Fig. 5. Schematic illustration of average surface and colloid properties of particle classes in the 10 mm – 10 nm range. Note that nano particle class 1 nm – 10 nm is excluded, since particles have abnormal properties.

the cohesion simultaneously increases. Such particles can be produced only by controlled synthesis. Due to gas/liquid-like behavior of colloid particles their (gas/liquid) suspensions are modeled as molecular assemblies (discussed later). The exceptional surface properties of nano particles in 1–10 nm range dominates over bulk properties and results in abnormal chemical and physical effects.

2.4. Particle size (class) – distributions

A proper sampling of powders is a difficult task since particles of different sizes segregate at standstill. Therefore, samples should be taken from mobile powders (conveyer belts) at different locations and at different times. For fine powders in air borne streams the sampling rate must be same as the feeding speed. The size distribution of nearly monodisperse powders is usually presented as fraction (per cent) of particles with a particular size of the total number of particles (Fig. 6) [5,9]. The most frequent particle size is denoted the *mode*. The 50% limit of cumulative particle size average is denoted *median*. It splits the distribution into two equal parts. The *mean* (\bar{s}) characterizes the center of gravity of the distribution. The average sizes can be related by moment mean as:

$$(mean-mode) = 3 (mean-median) \quad (13)$$

Eq. (13) does not apply for strongly asymmetric particle distributions.

Some relative particle sizes were defined in Table 5. As discussed, the distribution mean corresponds to the volume moment size ($\bar{s} = s_{VM}$). There are a vast number of methods developed to characterize multimodal size distributions [9]. A few methods to plot a tetramodal size distribution are illustrated in Fig. 7.

The *Phi* or *TP size scale* is mainly used in geology where each particle size segment is in one-fourth phi units:

$$s_{TP} = -\log_2 s_i \Leftrightarrow s_i = 2^{-s_{TP}} \quad (14)$$

where the relative size s_{TP} is a dimensionless particle size ratio between given and standard particle sizes. On *arithmetic normal (AN) distribution scale* all segments (expressed as s) are equally wide. The normal or bell-

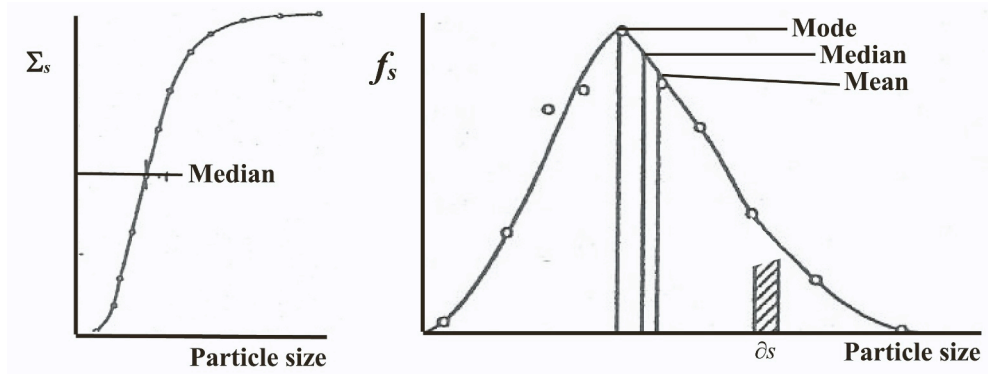


Fig. 6. Schematic illustration of cumulative particle size (Σ_s , left diagram) and of most frequent particle size (f_s , right diagram) plotted as a function of particle size. The mode, median and mean sizes are identified [9].

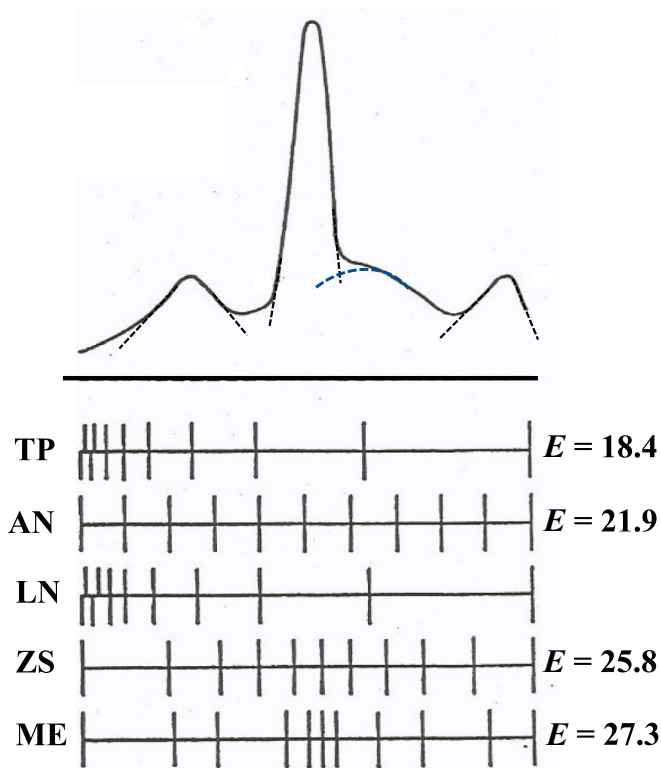


Fig. 7. Alternative methods to divide an arbitrary tetra-modal size distribution as phi (TP), arithmetic-normal (AN), logarithmic-normal (LN), zeta score (ZS) and maximum information entropy (ME) size segments [9]. The relative negentropy (E , Eq. (17)) value is indicated.

shaped Gaussian frequency distribution is characterized by a symmetric distribution of sizes around the mode. Assume a frequency of particle sizes where the cumulative results of small fractions, each contributing in the same degree to final distribution. Then particle size data would conform to the Gaussian distribution [9,14] as:

$$f_N = \frac{1}{\sqrt{2\pi}\sigma_N} e^{-(s-s_N)^2/2\sigma_N^2} \quad (15)$$

where f_N = probability density, s = particle size, s_N = arithmetic mean of particle diameters and σ_N = standard deviation. The mean diameter for Gaussian distribution corresponds to the mode (Fig. 6, Table 5) and the size around which the distribution is centered.

Eq. (15) results in a straight line when plotted linearly as a function of particle diameter. In Fig. 8 the f_N -axis represents a cumulative

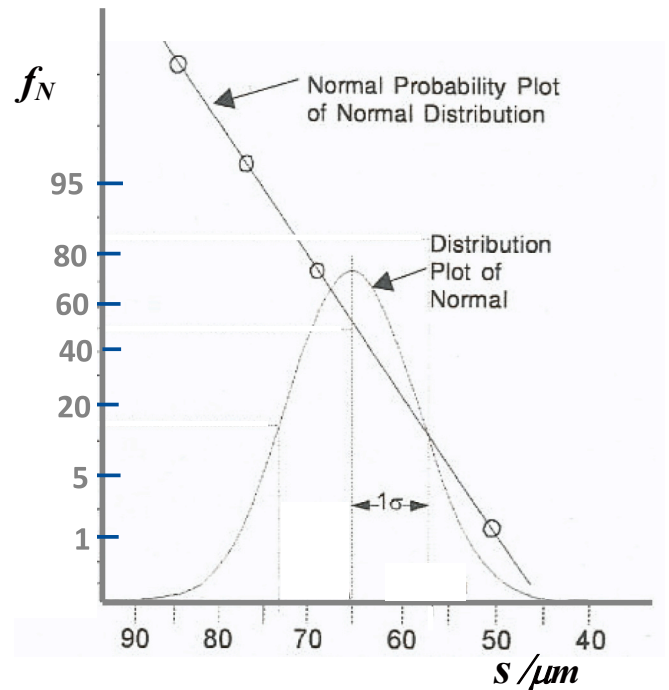


Fig. 8. Cumulative normal particle size distribution and normal probability density (f_N , Eq. (15)) plotted as a function of evenly distributed particle sizes (s) [14]. For details, consult [9].

quantity (Eq. (15)). The scale of f_N -axis is spaced corresponding to a normal distribution about the mode value [9,14]. Fig. 8 illustrates that a real normal distribution produces a straight line.

The slope of the straight line is related to the standard deviation (spread) of the distribution. Positions along the s -axis correspond to the mean and mode diameters and indicate the beginning and ending diameters of the distribution.

On logarithmic normal (LN) scale each size segment corresponds to logs. Attributing the source of particle creation to ratios of effects and not merely differences in excess or divergency from a mean value lead [14] to:

$$f_G = \frac{1}{\sqrt{2\pi}\log\sigma_G} e^{-(\log s - \log s_G)^2/2\log^2\sigma_G} \quad (16)$$

where s_G = geometric mean size and σ_G = geometric standard deviation. Many plots of particle mass distribution by size (nearly) produce a Gaussian-shaped curve only when plotted on a logarithmic diameter axis. It is then informative to have particle size data presented as a log-

probability plot where the probability function is derived from binomial theory [9,14]. Fig. 9 is an example of a log-probability plot overlaid onto a differential mass plot of the same data.

As with normal probability plot (Fig. 8), the *log probability plot* scale conforms to a normal distribution plotted as a function of logarithmic equivalent sphere size (s). If the measured particle diameters are log-normally distributed, the plot is linear. As shown, bimodal log-normal distributions produce two segments. Deviation from linearity in a particular range indicates deviation from a normal distribution in that range. The geometric mean diameter relates to *Phi* method representing the frequency of particles (mode) plotted against logs – normal (mass or number) distribution.

Zeta Score method is based on a maximum normal Gaussian probability distribution around the mean value. The distribution segments are therefore narrower when particle size density is largest. Log-normal methods are special cases of Zero Score (ZS) method. In the maximal information entropy (ME) method the information density is analyzed as negative product of probability (p) to find a particle size within segment i . The natural logarithm of probability is related to negentropy (E) as:

$$E = -\sum_i p_i \ln p_i \quad (17)$$

Summation is executed over all particle segments. Due to different number of particle sizes in each segment the average sizes vary accordingly. As shown in Fig. 7 the largest information density (negentropy) is achieved by maximum entropy size class distribution.

2.5. Summary

Division of a reference particle into an increased number of smaller sizes enhances the accumulated surface area as compared to the constant total volume. For mineral particles within 1–100 μm (micro-particle) size range the increased number of broken lattice surfaces increases attraction (catalytic activity) between crystal planes resulting in enhanced interparticle cohesion. Particles in 10 nm – 1 μm size range poses gas/liquid-like behavior and therefore colloid particle (gas/liquid) suspensions are modeled as molecular assemblies. The exceptional surface properties of nano particles in 1–10 nm size range dominates over bulk properties (if any) and results in abnormal chemical and physical effects.

Equivalent spheres can be derived for molecular species as well as for non-uniform model particles. Irregular particles may be represented by equivalent spheres. The degree of asymmetry is characterized by three-dimensional sphericity and projected on a plane by two-dimensional circularity. Depending on which property is experimentally determined the equivalent particle diameter differ considerably. Considering particle size classes two of their properties may be combined to determine rather different average diameters.

Most frequent particle size (*mode*) and 50% average (*median*)

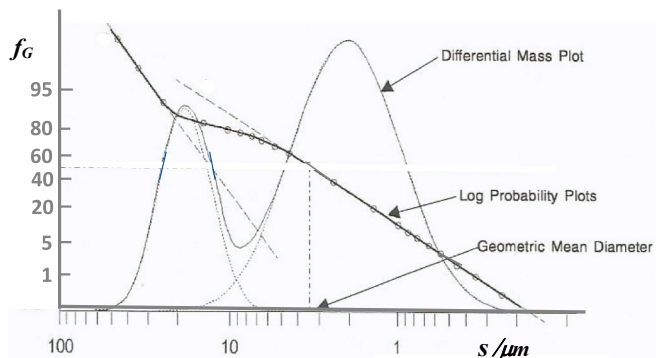


Fig. 9. Differential mass plots and geometric probability density (f_G , Eq. (16)) plotted as a function of logarithmic equivalent sphere diameter (s) [14]. For details, consult [9].

cumulative particle sizes can be related by calculated moment mean particle sizes for small particle distributions. Normal probability of mono- and multi-mode distributions may be characterized using Phi or TP, normal arithmetic (NA), logarithmic normal (LN), zeta score (ZS) and maximum information entropy (ME) particle size segments. Maximal information entropy (ME) of probability to find a particle size within a particular size segment may be applied to all size scales.

3. Packing of particles

In this section the attention is focused on packing of mono-, di- and tri-modal particles. Particles are considered as hard spheres without mutual interaction. Denotations and models used by “particle community” is rather confusing [15]. Therefore, their expressions and models are replaced by a straightforward physico-chemical framework. This provides improved opportunities for future modeling.

3.1. Packing of monodisperse hard spheres – porosity

Packing pattern are characterized by particle arrangements involving coordination (nearest neighbor) numbers (N_C) and particle volume fractions (ϕ_p). There are only four different basic packing arrangements based on square and simple rhombic or triangular unit cells (Fig. 10); cubic, orthorhombic, tetragonal–sphenoidal, and rhombohedral–hexagonal.

For any particular orientation, two successive layers of particle spheres will be a fixed distance apart (layer spacing) defined by particle radius or diameter (Figs.3 and 4). Unit cells are the smallest portion of the system that gives complete representation of packing arrangements and of the distribution of voids. Some alternative stackings (not discussed further) are moreover possible within the imposed conditions [15]. Key characteristics of basic particle packings are listed in Table 6.

Depending on mixing procedure there are additional experimentally determined packing densities:

- Very loose packing formed during settling, $\phi_{VLP} = 0.56$ ($\phi_{VLP}^{-1} = 1.79$)
- Random loose packing mixed by hand, $0.59 < \phi_{RLP} < 0.60$ ($1.67 < \phi_{RLP}^{-1} < 1.69$)
- Dense random close packing formed by pouring, $0.63 < \phi_{RCP} < 0.64$ ($1.56 < \phi_{RCP}^{-1} < 1.60$)

Hydrodynamic radii ($r_h = \pi r_a^2 / 2\pi r_{2D} = r_a/2$, r_a = pore radius) can be assigned for fictive capillaries (pores) through the packed particle matrix. The particle radius can be related to particle density and their specific surface area as: $\rho_p A_{sp} = 4\pi r_h^2 / (4\pi r_p^3 / 3) = 3/r_p$. The fictive pore diameter may be calculated [16,17] as:

$$d_v = 4r_h = 4 \frac{1 - \phi_p}{\rho_p A_{sp} \phi_p} = \frac{2}{3} d_p \left(\frac{1 - \phi_p}{\phi_p} \right) = \frac{2}{3} d_p \left(\frac{\varepsilon_v}{\phi_p} \right) = k_p d_p \quad (18)$$

where $\phi_p = V_p/V_t$ and $\varepsilon_v = V_v/V_t = 1 - \phi_p$. As shown in Eq. (18) the pore diameter in a regular particle matrix is only slightly smaller than the particle diameters. For irregular particles, the packing features may differ considerably. With this information at hand the nomenclature used by researchers investigating porous materials is rather contradictory. According to IUPAC [18]:

- Micropores, $d_v < 2$ nm
- Mesopores, $2 < d_v < 50$ nm
- Macropores, $d_v > 50$ nm

Moreover, denotations as ultra-micropores, $d_v < 0.7$ nm and secondary micropores, $0.7 < d_v < 2$ nm are used. Fortunately, micropores have recently been renamed nanopores.

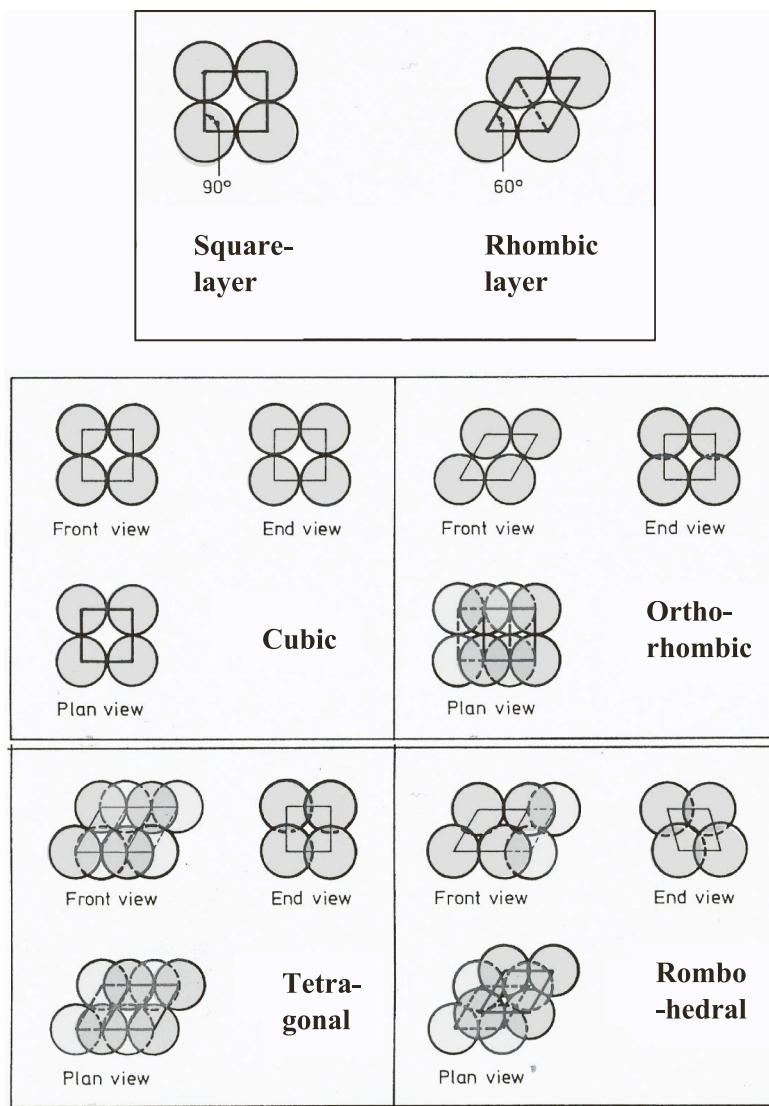


Fig. 10. Upper doublet: Hard spheres in square (left) and simple rhombic (right) arrangements. Lower figures: Cubic, orthorhombic, tetragonal(–sphenoidal), and rhombohedral(–hexagonal) stacking of hard spheres [15].

Table 6

Coordination numbers (N_C), unit cell volumes (v_c) expressed as sphere radius ($v_c(r)$), particle fraction (ϕ_p), void fraction (porosity, ϵ_v), void/particle ratio (ϵ_v/ϕ_p), layer spacing (l_r) and numerical layer spacing per diameter ($l_r/2r$) [15].

Packing	N_C	v_c	ϕ_p	ϵ_v	ϵ_v/ϕ_p	l_r	$l_r/2r$
Cubic	6	$8r^3$	0.5236	0.4764	0.9098	$2r$	1.000
Orto- rombic	8	$4(3)^{1/3} 2r^3$	0.6046	0.3954	0.6540	$2r$	1.000
Tetragonal	10	$6r^3$	0.6981	0.3019	0.4325	$(3)^{1/2}r$	0.866
Rhombo- hedral	12	$4(2)^{1/3} 2r^3$	0.7405	0.2595	0.3504	$(2)^{1/2}r$	0.708
	12	$4(2)^{1/3} 2r^3$	0.7405	0.2595	0.3504	$2(2/3)^{1/3} 2r$	0.816

3.2. Bimodal particle mixing and packing

To visualize the influence of packing, different sized particles individual partial properties are introduced. The deviation from their monomodal ideal packing is expressed as partial mixing functions. The maximum packing density is modeled separately for large (coarse),

medium and small (fine) particles. The deviation of experimental packing from the modeled maximum packing is expressed by excess values. The dependence of ultimate packing density on particle size ratio and composition is evaluated.

3.2.1. Partial properties

When mixing reasonably spherical particles, their mass (m_p/g) and density ($\rho_p/(g/cm^3)$) are usually known. This allows definition of total (mass dependent) binary particle volume (cm^3) in terms of partial specific volumes ($v_i/(cm^3/g)$) as:

$$V_p = m_p v_p = \frac{m_1}{\rho_1} + \frac{m_2}{\rho_2} = m_1 v_1 + m_2 v_2 \Leftrightarrow v_i = \left(\frac{\partial V_p}{\partial m_i} \right)_{m_j} \quad (19)$$

where $v_i \neq v_i^*$. The latter specific partial volume represents single (pure) particles. It is more convenient to express specific particle volume in terms of weight fractions (w_i) as:

$$v_p = w_1 v_1 + w_2 v_2 = v_1 + w_2(v_2 - v_1) \Leftrightarrow w_i = \frac{m_i}{m_1 + m_2} \quad (20)$$

where $w_1 = 1 - w_2$. Since $dw_1 = -dw_2$:

$$dv_p = dw_1 v_1 + dw_2 v_2 = dw_2 (v_2 - v_1) \Leftrightarrow \left(\frac{\partial v_p}{\partial w_2}\right) = (v_2 - v_1) \quad (21a)$$

Alternatively (Eq. (20)):

$$\left(\frac{\partial v_p}{\partial w_2}\right) = (v_2 - v_1) + \left[w_1 \left(\frac{\partial v_1}{\partial w_2}\right) + w_2 \left(\frac{\partial v_2}{\partial w_2}\right)\right] = (v_2 - v_1) \quad (21b)$$

Inserted into Eq. (20) we may extract v_1 as:

$$v_1 = v_p - w_2 \left(\frac{\partial v_p}{\partial w_2}\right) = v_p - w_2 (v_2 - v_1) \quad (22a)$$

From Eq. (21a) v_2 may be extracted as:

$$v_2 = v_1 + \left(\frac{\partial v_p}{\partial w_2}\right) \Leftrightarrow v_2 = v_p + (1 - w_2) \left(\frac{\partial v_p}{\partial w_2}\right) = v_p + w_1 (v_2 - v_1) \quad (22b)$$

As illustrated in Fig. 11 and in Eq. (22a) the tangent of v_p at $w_2 = 0$ equals v_1 and at $w_2 = 1$ v_p equals v_2 . In absence of particle mass data, water ($M_W = 18.015$ g/mol, $\rho_W^{25} = 0.99705$ g/cm³, $v_W^* = 1.00296$ cm³/g, $v_W^{*25} = 300,012 \cdot 10^{-29}$ m³, $d_W^{25} = 0,3855$ nm) – ethanol ($M_E = 46,068$ g/mol, $\rho_E^{25} = 0.78504$ g/cm³, $v_E^* = 1.27382$ cm³/g, $v_E^{*25} = 9.74382 \cdot 10^{-29}$ m³, $d_E^{25} = 0,5709$ nm) mixtures are used as example. Their volume ratio is 3.245 and their diameter ratio is 1.482.

One may define a mixing function (M) with reference to limiting (pure, v_i^*) specific volumes as:

$$v_p^M = w_1 (v_1 - v_1^*) + w_2 (v_2 - v_2^*) = w_1 v_1^M + w_2 v_2^M \quad (23)$$

The partial specific volumes of mixing are presented in right diagram of Fig. 11. A negative contribution (reduced volume from ideality) characterizes improved water – ethanol interaction in excess over water – water or ethanol – ethanol interactions. This is indeed realized for both components, particularly for ethanol at small w_E and increasingly for water when w_E increases.

It has become a practice to characterize particle mixtures in terms of particle volume fractions (ϕ_p). Since $m_i/\rho_i = m_i v_i^* = v_i^*$ (Eq. (19)) we may write for particle volume V_p (cm³):

$$V_p = \varphi_1 V_p + \varphi_2 V_p = \left(\frac{v_1^*}{v_1^* + v_2^*}\right) V_p + \left(\frac{v_2^*}{v_1^* + v_2^*}\right) V_p \quad (24)$$

The reduced volume fractions (φ_i) are expressed only in terms of particle volumes excluding contribution of voids. Considering particles embedded in a cylinder (total $V_t = \pi r^2 h$) the sum of volume fractions of voids ($\phi_v = V_v/V_t$) and particles ($\phi_p = V_p/V_t$) equals unity. Considering volume fraction of particles (Eq. (20)):

$$1 - \phi_v = \phi_p = \varphi_1 \phi_1 + \varphi_2 \phi_2 \quad (25)$$

where ϕ_i are partial volume fractions ($\neq \phi_i^*$, single (pure) particles). Table 7 lists the volume fractions of pores (porosity, ε_v) and of monomodal particles of a wide size range.

As shown the packing (volume fraction) is nearly independent of particle sizes (except for fine sand) and remain between orthorhombic

Table 7

Porosity (ε_v) and volume fraction of monomodal particles ($\phi_p = \phi_i^*$, single (pure) particles) of a wide range of densities (ρ_p /(g/cm³)) and sizes (d_p /mm) packed in a cylinder of unit volume [19].

Particles	ρ_p	d_p	ε_v	ϕ_p	$1/\phi_p$
Lead shots	11.25	4.826	0.369	0.631	1.585
Lead shots	11.25	3.810	0.369	0.631	1.585
Lead shots	11.25	2.794	0.370	0.630	1.587
Lead shots	11.25	1.778	0.369	0.631	1.585
Steal bearings	7.87	7925	0.392	0.608	1.645
Coarse sand	2.69	4.47	0.377	0.623	1.605
Medium sand	2.76	0.711	0.382	0.618	1.618
Fine sand	2.75	0.089	0.425	0.575	1.739

and tetragonal packing (Table 4). It has been observed that the preferential packing is horizontally tetragonal and vertically cubic ($\phi_v = 0.395$, $\phi_p = 0.605$, $1/\phi_p = 1.653$) [15].

Since $\varphi_M + \varphi_F = 1$ Eq. (25) may for mixing of medium-fine particles be rewritten (Eq. (20)) as:

$$\phi_p = \phi_M + \varphi_F (\phi_F - \phi_M) \Leftrightarrow \left(\frac{\partial \phi_p}{\partial \varphi_F}\right) = (\phi_F - \phi_M) \quad (26)$$

According to Eqs. (22a) and (22b) we may write for their partial derivatives:

$$\phi_M = \phi_p - \varphi_F \left(\frac{\partial \phi_p}{\partial \varphi_F}\right) = \phi_p - \varphi_F (\phi_F - \phi_M) \quad (27a)$$

$$\phi_F = \phi_p + (1 - \varphi_F) \left(\frac{\partial \phi_p}{\partial \varphi_F}\right) = \phi_p + \varphi_M (\phi_F - \phi_M) \quad (27b)$$

Alike in Fig. 11, extraction of partial (inverse) particle volume fraction (ϕ_p, ϕ_p^{-1}) contributions of a binary mixture of medium ($d_M = 0.711$ mm) and fine ($d_F = 0,089$ mm) roughly spherical sand particles (Table 7) at $\varphi_F = 0.25$ is presented in Fig. 12.

Partial particle volume fractions (ϕ_p) is plotted in Fig. 13 as a function of reduced volume fraction (φ_F) of fine particles.

Alternatively, the model may be based on inverse particle volume fractions (Eq. (25)) as:

$$1/\phi_p = \phi_p^{-1} = \varphi_M \phi_M^{-1} + \varphi_F \phi_F^{-1} \quad (28)$$

where $1/\phi_i$ are partial inverse partial volumes ($\neq 1/\phi_i^*$, Table 7). The unconventional approach used within “particle community” to denote inverted volume fractions dimensionless apparent volumes (V_a) [15] is confusing. Written in terms of partial contributions (Eqs. (27a),(27b)) we find that:

$$\phi_M^{-1} = \phi_p^{-1} - \varphi_F \left(\frac{\partial \phi_p^{-1}}{\partial \varphi_F}\right) = \phi_p^{-1} - \varphi_F (\phi_F^{-1} - \phi_M^{-1}) \quad (29a)$$

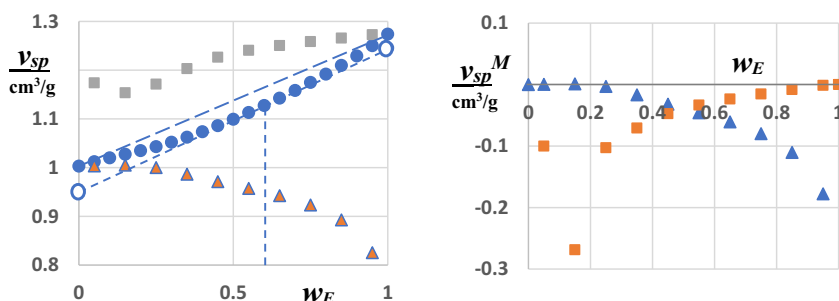


Fig. 11. Left diagram: Specific volume ($v_{sp}/(\text{cm}^3/\text{g})$, filled circles) and partial specific volumes of water (triangles) – ethanol (squares) mixtures plotted as a function of weight fraction ethanol (w_E). Ideal mixing is indicated as a dashed line between end points. The partial contributions (open circles) are extracted using the slope, $dv_{mix}/dw_E = 0.295$ at $w_E = 0.6$ (dotted line). According to Eq. (22a) $v_W = 0.950$ at $w_E = 0$ and Eq. (22b) $v_E = 1.246$ at $w_E = 1$ [3]. Right diagram: Corresponding partial specific volume of mixing (deviation from ideality, Eq. (23)).

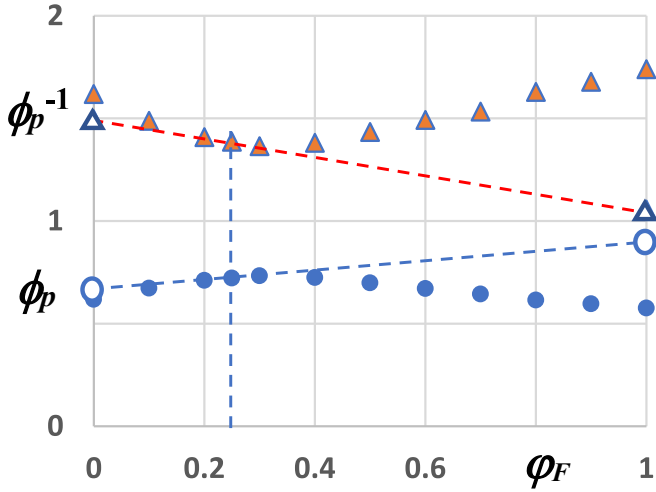


Fig. 12. Volume fractions (ϕ_p , circles) and inverted volume fractions ($1/\phi_p = \phi_p^{-1}$, triangles) of mixtures of medium ($d_M = 0.711$ mm) and fine ($d_F = 0.089$ mm) particles plotted against reduced volume fraction of fine particles (φ_F). Partial contributions are extracted at $\varphi_F = 0.25$ (open symbols, dotted lines) using the slope $d\phi_p/d\varphi_F = 0.23$ and $d\phi_p^{-1}/d\varphi_F = -0.44$, respectively. According to Eq. (27a) $\phi_M = 0.664$ at $\varphi_F = 0$ and Eq. (27b) $\phi_F = 0.894$ at $\varphi_F = 1$. According to Eq. (29a) $1/\phi_M = 1496$ at $\varphi_F = 0$ and Eq. (29b) $1/\phi_F = 1056$ at $\varphi_F = 1$.

$$\phi_F^{-1} = \phi_p^{-1} + (1 - \varphi_F) \left(\frac{\partial \phi_p^{-1}}{\partial \varphi_F} \right) = \phi_p^{-1} + \varphi_M (\phi_F^{-1} - \phi_M^{-1}) \quad (29b)$$

Partial inverse particle volume fractions (ϕ_i^{-1}) are plotted in Fig. 13 as a function of reduced volume fraction (φ_F) of fine particles.

Volume fractions reach a maximum (ϕ_{max}) or minimum (ϕ_{min}^{-1}) when $0.25 < \varphi_F < 0.45$. The partial packing contribution of fine particles is greatest when $\varphi_F < 0.3$ and is thereafter reduced to nearly ideal inverse volume fractions. The partial packing contribution of medium particles is initially nearly on ideal level but is enhanced when $\varphi_F > 0.2$.

The ideal mixing of medium and fine particles may be used as a reference for evaluations:

$$\phi_p^{id} = (1 - \varphi_F)\phi_M^* + \varphi_F\phi_F^* \quad (30)$$

where ϕ_M^* , ϕ_F^* represent volume fractions of each single particle type (Table 7). The straight-line (diamonds) connecting intercept values in Fig. 13 represents ideal mixing. The degree of compression due to enhanced mixing may be expressed as the deviation from single particle packing values (ϕ_M^* , ϕ_F^*) as mixing (M) functions:

$$\begin{aligned} \phi_p^M &= (1 - \varphi_F)(\phi_M - \phi_M^*) + \varphi_F(\phi_F - \phi_F^*) = \\ &= (1 - \varphi_F)\phi_M^M + \varphi_F\phi_F^M = \phi_p(\varphi_F) - \phi_p^{id}(\varphi_F) \end{aligned} \quad (31)$$

Volume fractions of mixing and partial volume fractions of mixing are illustrated in Fig. 14. As shown, the observations made in Fig. 13 are confirmed and quantified on an expanded scale. As shown, the total volume fraction of mixing is characterized by increased packing efficiency (positive ϕ_p deviation). Optimal mixing conditions appear at $0.25 < \varphi_F < 0.45$ (location of ϕ_p^M maximum). Obviously, mutual mixing ($M \leftrightarrow F$ packing) is at all proportions more favourable than fractional contribution of individual particle ($M \leftrightarrow M, F \leftrightarrow F$) packing. As shown in left diagrams of Fig. 14 packing contribution of medium particles is enhanced by the presence of fine particles when $\varphi_F > 0.25$. This limit corresponds probably to fine particles filling the voids between medium particle clusters. When $\varphi_F > 0.45$ medium particles become immersed in fine particles the partial volume fraction of mixing is stabilized at a rather constant ϕ_M^M value. The opposite applies for fine particles for which mutual effective void packing is successively reduced within $0 < \varphi_F < 0.45$ to the ideal level. Thereafter immersion of medium particles does not influence markedly the packing efficiency of fine particles.

The corresponding ideal mixing of medium and fine particles as a function of reduced volume fraction of fine particles (φ_F) may be used as a reference:

$$(\phi_p^{-1})^{id} = (1 - \varphi_F)(\phi_M^*)^{-1} + \varphi_F(\phi_F^*)^{-1} \quad (32)$$

where $((\phi_M^*)^{-1}, (\phi_F^*)^{-1})$ represent inverse volume fractions of each single particle type (Table 7). The straight-line connecting intercept values (diamonds) in Fig. 13 represents ideal mixing. The degree of shrinking due to mixing (M) may be expressed as the deviation of experimental values from this ideal mixing as:

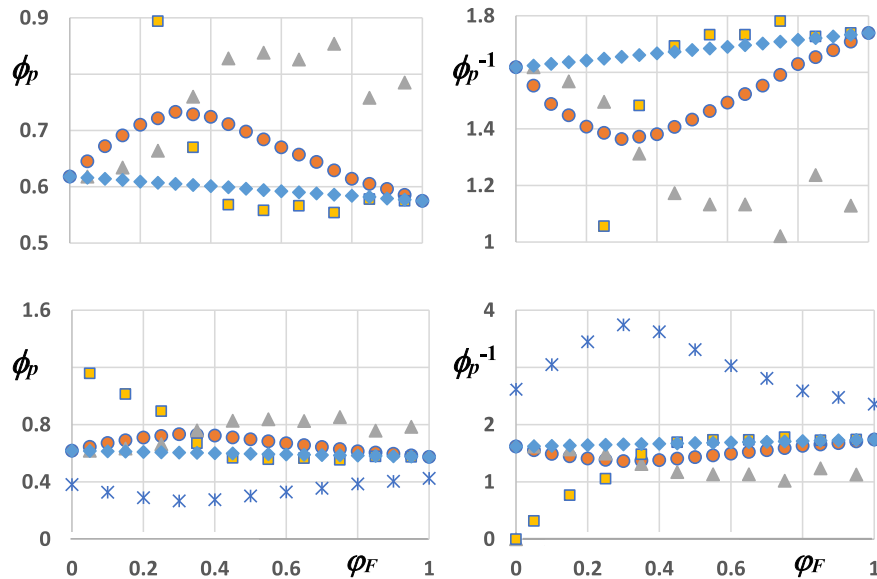


Fig. 13. Left diagrams: Porosity (ϵ_v , asterisks) and volume fractions (ϕ_p , circles) of mixed medium and fine particles. Partial volume fractions (medium ϕ_M triangles, fine ϕ_F squares) and ideal volume fraction of mixing (diamonds) plotted as a function of reduced volume fraction of fine particles (φ_F). Right diagrams: Corresponding dependencies of inverse volume fractions (ϕ_p^{-1}). Upper diagrams: Volume fraction scale expanded.

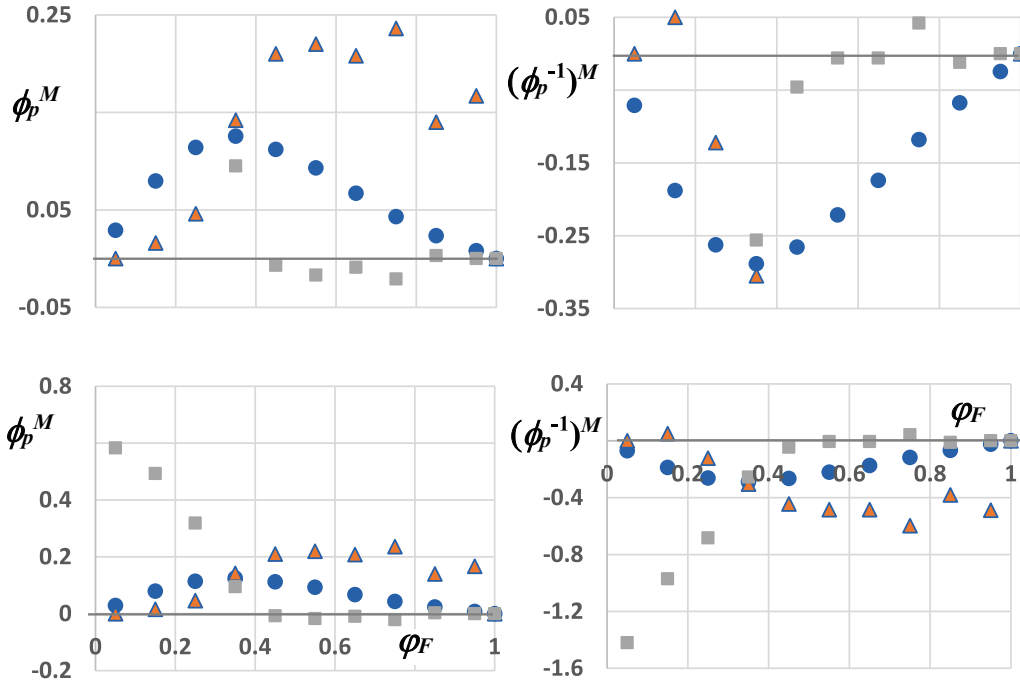


Fig. 14. Left diagrams: Volume fraction of mixing medium and fine particles (ϕ_p^M , circles, Eq. (31)) and partial volume fractions of mixing (medium ϕ_M^M , triangles, fine ϕ_F^M , squares) particles plotted as a function of reduced volume fraction of fine particles (φ_F). Right diagrams: Corresponding dependencies of inverse volume fractions of mixing ($(\phi_p^M)^{-1}$, circles, Eq. (33) medium $(\phi_M^M)^{-1}$, triangles, fine $(\phi_F^M)^{-1}$, squares). Upper diagrams: Volume fraction scale expanded.

$$\begin{aligned}
 (\phi_p^{-1})^M &= (1 - \varphi_F) [\phi_M^{-1} - (\phi_M^\bullet)^{-1}] + \varphi_F [\phi_F^{-1} - (\phi_F^\bullet)^{-1}] = \\
 &= (1 - \varphi_F)(\phi_M^{-1})^M + \varphi_F(\phi_F^{-1})^M = (\phi_p^{-1})^{\text{exp}}(\varphi_F) - (\phi_p^{-1})^{\text{id}}(\varphi_F)
 \end{aligned}
 \tag{33}$$

Experimental inverse mixing volume fractions and ideal inverse volume fractions are illustrated in Fig. 14. The interpretation of volume fractions of mixing seems more straightforward as compared to inverse functions characterized by negative deviations.

3.2.2. Models for binary particle mixing

Packing models assume that smaller particles are filling the voids between larger particles (Fig. 15). Alternatively large particles are immersed in smaller particles. This results in loss of one dimension of packing freedom (excluded volume).

When large (coarse, medium) particles dominate for small (medium, fine) φ_S one finds that [20–22]:

$$(\phi_p)_L^N = \frac{\phi_L^\bullet}{1 - \varphi_S}
 \tag{34a}$$

For large particles $\phi_L^\bullet = \phi_C^\bullet = 0.623$ or $\phi_L^\bullet = \phi_M^\bullet = 0.618$ (Table 7). When small particles dominate for large φ_S one finds that [20–22]:

$$(\phi_p)_S^N = \frac{\phi_S^\bullet}{\varphi_S + \phi_S^\bullet(1 - \varphi_S)}
 \tag{34b}$$

For small particles $\phi_S^\bullet = \phi_M^\bullet = 0.618$ or $\phi_S^\bullet = \phi_F^\bullet = 0.575$ (Table 7). These nonlinear (N) models are fitted to experimental results in Fig. 16.

The nonlinear models predict the changes of volume fraction quite accurately and cross each other around a maximum (ϕ_{max}) at $2.7 < \varphi_S < 3.0$, which agrees roughly with experimentally observed ϕ_p values but the overall fit depends on d_L/d_S . The fit of measured ϕ_p curve as function of φ_S ($S = M, F$) seems to be optimal close to ϕ_p saturation at $d_L/d_S = 50$, as judged from non-existent wedging (void contribution). The two models thus explain the enhanced packing enhancement due to mixing large and small particles. The larger the particle size difference is, the larger is packing efficiency and the better is predictivity of the models. It is quite remarkable that the packing density of large particles alone (ϕ_L^\bullet , $L = M, C$) can predict the enhanced packing at low φ_S ($S = M, F$). The packing density of small particles alone (ϕ_S^\bullet , $S = M, F$) can, on the other hand successfully explain the increased packing density at large φ_S .

The predicted cross-point can be evaluated using Eqs. (34a) and

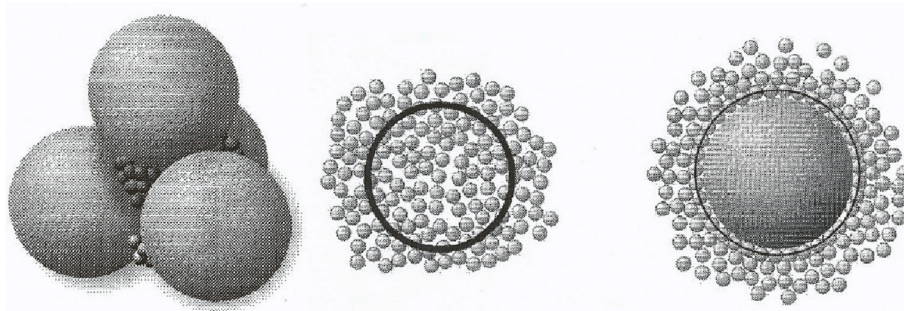


Fig. 15. When small particles fill the voids between large particles (left) and large particles replace small particles (middle) a wall effect appear due to the loss of one degree of packing freedom (right).

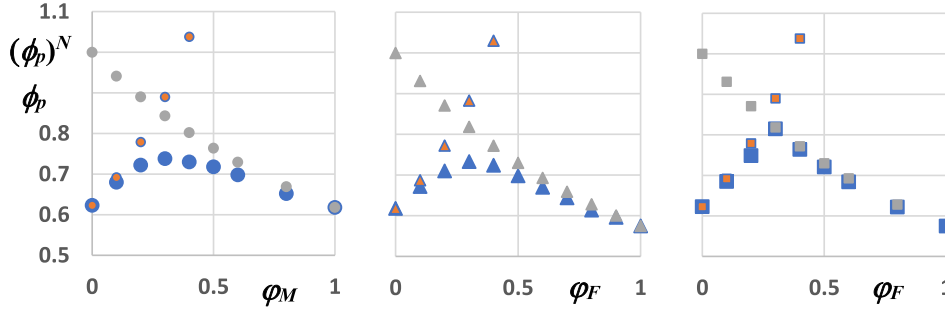


Fig. 16. Fit of non-linear models ($(\phi_p)^N$, Eqs. (34a) left, (34b) right, small symbols) to volume fractions (ϕ_p) of course – medium (circles, $d_C/d_M = 6.3$, left diagram), medium – fine (triangles, $d_C/d_M = 8.0$ middle diagram) and coarse – fine (squares, $d_C/d_M = 50$ right diagram) particle mixtures.

(34b) since both ϕ_p and φ_S equal at this point. By eliminating φ_S we find that:

$$\phi_{\max}^N = 2\phi_p^* - (\phi_p^*)^2 \quad (35a)$$

where ϕ_p^* is given by the system investigated. By eliminating ϕ_p we find that:

$$\varphi_{\max}^N = \frac{\phi_p^* - (\phi_p^*)^2}{2\phi_p^* - (\phi_p^*)^2} \quad (35b)$$

The results for model systems are;

- For the coarse – medium system ($d_C/d_M = 6.3$) the model predicts that $\phi_C^N = 0.858$ (Eq. (35a)) at $\varphi_M^N = 0.274$ (Eq. (35b)) and that $\phi_M^N = 0.854$ (Eq. (35a)) at $\varphi_M^N = 0.276$ (Eq. (35b)). The highest experimental point found is $\phi_p = 0.738$ at $\varphi_M = 0.3$.
- For the medium – fine system ($d_M/d_F = 8.0$) the model predicts that that $\phi_M^N = 0.854$ (Eq. (35a)) at $\varphi_F^N = 0.276$ (Eq. (31b)) and that $\phi_F^N = 0.819$ (Eq. (35a)) at $\varphi_F^N = 0.298$ (Eq. (35b)). The highest experimental point found is $\phi_p = 0.733$ at $\varphi_F = 0.3$.
- For the coarse – fine system ($d_C/d_F = 50$) the model predicts that $\phi_C^N = 0.858$ (Eq. (35a)) at $\varphi_F^N = 0.274$ (Eq. (35b)) and that $\phi_F^N = 0.819$ (Eq. (35a)) at $\varphi_F^N = 0.298$ (Eq. (35b)). The highest experimental point found is $\phi_p = 0.815$ at $\varphi_M = 0.3$.

Although model fits are very good, the highest experimental point is slightly off the location of maximum cross-over point.

Linear dependencies of inverse volume fraction (ϕ_p^{-1} , representing apparent volume, V_a) models are based on mixtures of monodisperse spherical particles but serves as a reference for polydisperse non-spherical particle mixtures. Initially the d_L/d_S ratio is unity and $\phi_p^{-1} = (\phi_p^*)^{-1} - 1$ at $\varphi_S = 0$ [15]. It is assumed small particles fill the voids between large particles (onward direction) and $\phi_p^{-1} = (\phi_p^*)^{-1} - 0$ at $\varphi_S = 1$. For mixtures of large (L) and small (S) particles (Table 7) the equation for straight lines gives for the onward direction:

$$\phi_p^{-1} = \phi_{p,0}^{-1} + \left(\frac{\phi_{p,0}^{-1} - \phi_{p,1}^{-1}}{\varphi_{S,0} - \varphi_{S,1}} \right) (\varphi_S - \varphi_{S,0}) = \phi_{p,0}^{-1} - \phi_{p,0}^{-1} \varphi_S \quad (36a)$$

and:

$$\phi_p^{-1} = \phi_{p,1}^{-1} + \left(\frac{\phi_{p,1}^{-1} - \phi_{p,0}^{-1}}{\varphi_{S,1} - \varphi_{S,0}} \right) (\varphi_S - \varphi_{S,1}) = \phi_{p,1}^{-1} + (\phi_{p,1}^{-1} - 1)(\varphi_S - 1) \quad (36b)$$

in reversed direction. Introducing volume fractions for coarse and medium ($d_C/d_M = 6.3$) sand fractions we find for the linear (L) model that:

$$(\phi_p^{-1})_C^L = (\phi_C^*)^{-1} - \varphi_M (\phi_C^*)^{-1} \quad (37a)$$

$$(\phi_p^{-1})_F^L = (\phi_M^*)^{-1} + (\varphi_M - 1) [(\phi_M^*)^{-1} - 1] = 1 + \varphi_M [(\phi_M^*)^{-1} - 1] \quad (37b)$$

Introducing volume fractions for medium and fine ($d_M/d_F = 8.0$) sand fractions we find for the linear (L) model that:

$$(\phi_p^{-1})_M^L = (\phi_M^*)^{-1} - \varphi_F (\phi_M^*)^{-1} \quad (38a)$$

$$(\phi_p^{-1})_F^L = (\phi_F^*)^{-1} + (\varphi_F - 1) [(\phi_F^*)^{-1} - 1] = 1 + \varphi_F [(\phi_F^*)^{-1} - 1] \quad (38b)$$

Introducing volume fractions for coarse and fine ($d_C/d_F = 50$) sand fractions we find for the linear (L) model that:

$$(\phi_p^{-1})_C^L = (\phi_C^*)^{-1} - \varphi_F (\phi_C^*)^{-1} \quad (39a)$$

$$(\phi_p^{-1})_F^L = (\phi_F^*)^{-1} + (\varphi_F - 1) [(\phi_F^*)^{-1} - 1] = 1 + \varphi_F [(\phi_F^*)^{-1} - 1] \quad (39b)$$

Note that these dual inverse volume fractions are total, but not partial properties. Model plots are presented in Fig. 17.

The linear models predict the changes of inverse volume fraction quite accurately and cross each other around a minimum (ϕ_{\min}^{-1}) at $2.5 < \varphi_S < 2.8$, which agrees roughly with experimentally observed ϕ_p values but the overall fit depends on d_L/d_S (Fig. 17). The fit of measured ϕ_p^{-1} curve as function of φ_S seems to be optimal close to saturation (ϕ_{sat}^{-1}) at $d_L/d_S = 50$, as judged from non-existent wedging (void contribution).

The two models thus explain successfully the enhanced packing efficiency caused by mixing large and small particles. The larger the particle size difference is, the larger is packing density and the better is predictivity of the models. It is quite remarkable that the packing density of large particles alone, $(\phi_L^*)^{-1}$ can predict the enhanced packing disturbance at low φ_S . The packing density of small particles alone, $(\phi_S^*)^{-1}$ can on the other hand successfully explain the increased packing density at large φ_S (small φ_L). The deviation of experimental inverse partial volume of mixing from model predictions (voids contribution) may be expressed as excess functions. For mixtures of medium and fine particles the excess (E) functions may be written as:

$$(\phi_p^{-1})_L^E = (\phi_p^{-1})_L^L(\varphi_S) - \phi_p^{-1}(\varphi_S) \quad (40a)$$

$$(\phi_p^{-1})_S^E = (\phi_p^{-1})_S^L(\varphi_S) - \phi_p^{-1}(\varphi_S) \quad (40b)$$

Excess functions for medium and fine particle system are plotted in Fig. 18 as a function of reduced volume fraction of fine particles.

The larger particle size ratio is, the better is the model fit and the smaller is the excluded volume correction. The excess (deviation) needs only to be recorded until crossing point of linear medium (large, L) and

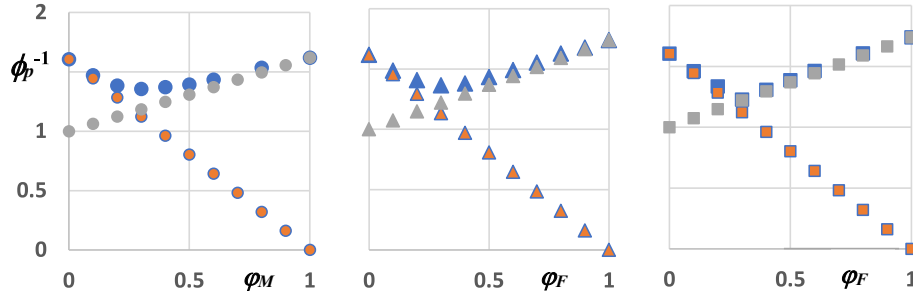


Fig. 17. Inverse volume fraction (ϕ_p^{-1}) of coarse and medium (circles, $d_C/d_M = 6.3$, left diagram), medium and fine (triangles, $d_C/d_M = 8.0$, middle diagram), coarse and fine (squares, $d_C/d_F = 50$, right diagram) particle mixtures plotted as a function of reduced medium (left, diagram) and of fine (middle and right diagram) particle fractions. Model fits: Eqs. (37a)-(37b) small spheres, Eqs. (38a)-(38b) small triangles, Eqs. (39a)-(39b) small squares.

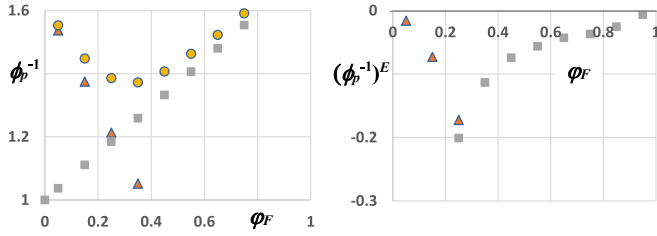


Fig. 18. Left diagram: Experimental inverse volume fraction of medium and fine particle mixtures (circles, Fig. 17). Linear model prediction medium particle branch (triangles, Eq. (38a)) and linear prediction of fine particle branch (squares, Eq. (38b)). Right diagram: Excess (deviation) of predicted inverse volume fractions from experimental medium (triangles, Eq. (40a)) and fine (squares, Eq. (40b)) particle branches.

fine (small, S) particle branches. The crossing point of model fits (φ_{min}) gives the reduced volume fraction of the optimal (densest packed, ϕ_{min}^{-1}) particle mix. Eqs. (37a)-(39b) can be generalized as:

$$(\phi_p^{-1})_L^L = (\phi_L^*)^{-1} - \varphi_S (\phi_S^*)^{-1} \quad (41a)$$

$$(\phi_p^{-1})_S^L = (\phi_S^*)^{-1} + (\varphi_S - 1) [(\phi_S^*)^{-1} - 1] = 1 + \varphi_S [(\phi_S^*)^{-1} - 1] \quad (41b)$$

where larger particles (C , M) are denoted L and smaller (M , F) particles are denoted S . Eliminating φ_S , we recover the minimum inverse volume fraction as:

$$\phi_{p,min}^{-1} = \frac{(\phi_L^*)^{-1} (\phi_S^*)^{-1}}{(\phi_L^*)^{-1} + (\phi_S^*)^{-1} - 1} \quad (42a)$$

Eliminating ϕ_p^{-1} , we find the coordinate of this minimum as:

$$\varphi_{S,min} = \frac{(\phi_L^*)^{-1} - 1}{(\phi_L^*)^{-1} + (\phi_S^*)^{-1} - 1} \quad (42b)$$

We may now compare the model prediction with the experimentally found minimum values in Fig. 17:

- Coarse-medium model ($d_M/d_M = 6.3$) $\phi_{p,min}^{-1} = 1.168$ at $\varphi_M = 0.272$ and experimentally $\phi_{p,min}^{-1} = 1.355$ at $\varphi_M = 0.3$.
- Medium-fine model ($d_M/d_F = 8.0$) $\phi_{p,min}^{-1} = 1.194$ at $\varphi_F = 0.262$ and experimentally $\phi_{p,min}^{-1} = 1.364$ at $\varphi_F = 0.3$ (Fig. 13).
- Coarse-fine model ($d_M/d_F = 50$) $\phi_{p,min}^{-1} = 1.191$ at $\varphi_F = 0.258$ and experimentally $\phi_{p,min}^{-1} = 1.227$ at $\varphi_F = 0.3$.

3.2.3. Dependence on particle size ratios

Fig. 19 shows the dependence of (inverted) volume fraction (ϕ_p , ϕ_p^{-1}) plotted as a function of d_L/d_S where $d_L = 3.15$ mm and $0.04 < d_S/\text{mm} < 1.55$ (metal shots, triangles and squares) or $d_L = 4.47$ mm (sand

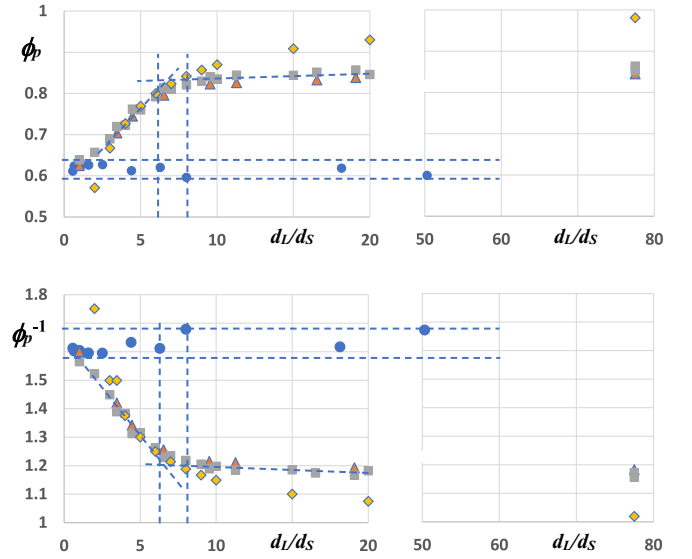


Fig. 19. Single (circles [15,19]), binary experimental (triangles [15,23]), corrected (squares [15,24]) and hydrodynamic (diamonds, Eq. (43)) particle volume fractions (ϕ_p , upper diagrams) and inverse volume fractions (ϕ_p^{-1} , lower diagrams) of packed steel metal shots and sand plotted as a function of the ratio between large and small particle diameters (d_L/d_S). Levels of random loose packing ($\phi_{RLP} = 0.595$, $\phi_{RLP}^{-1} = 1.68$) and random close packing ($\phi_{RCP} = 0.65$, $\phi_{RCP}^{-1} = 1.58$) indicated.

particles, circles) and $0.09 < d_S/\text{mm} < 7.92$ [15,19,23,24]. The levels for random loose packing ($0.59 < \phi_{RLP} < 0.60$, $1.67 < \phi_{RLP}^{-1} < 1.70$) and random close packing ($0.63 < \phi_{RCP} < 0.64$, $1.56 < \phi_{RCP}^{-1} < 1.57$) of monodisperse spheres are indicated.

Increasing particle size ratio (d_L/d_S) the packing densities of binary systems exceed by far the maximum packing density of single particle systems ($\phi_{p,max} = 0.741$, $\phi_{p,max}^{-1} = 1.35$). The less the diameter of small particles as compared to large particles is, the greater is ϕ_p and the smaller is wedging (pore volume). The break point between fast and slow change of (inverted) volume fraction is located at $6.5 < d_L/d_S < 7.0$ which corresponds to triangular pores between three large particles. The limiting condition for dense packing is that voids between large particles are sufficient for small particles to migrate to equilibrium positions. Above break point ($d_L/d_S > 7$) the migration of small particles become free and therefore volume fractions become nearly independent on d_L/d_S . Note that one model system (Table 7) is below or at this break point ($d_C/d_M = 6.29$), one is slightly above break point ($d_M/d_F = 7.99$), and one is close to saturation point ($d_C/d_F = 50.2$). The hydrodynamic model (Eq. (18)) predicted that this limit is reached at:

$$d_v = \frac{2}{3} \left(\frac{1}{\phi_p} - 1 \right) d_p \Leftrightarrow \frac{d_L}{d_S} \approx \frac{d_p}{d_v} = \frac{3}{2} \left(\frac{\phi_p}{1 - \phi_p} \right) \Leftrightarrow \phi_p = \frac{(d_L/d_S)}{1.5 + (d_L/d_S)} \quad (43)$$

For cubic dense packing of single particles $d_L/d_S = 1.649$, for orthorhombic packing $d_L/d_S = 2.294$, for tetragonal packing $d_L/d_S = 3.469$ and for rhombohedral packing $d_L/d_S = 4.280$. The dependence of (inverted) volume fraction on d_L/d_S is inserted in Fig. 19. The agreement with experimental values is particularly good within $3 < d_L/d_S < 7$. Depending on mixing method there are additional experimentally determined packing densities. Limiting values for dense packing may also be deduced on geometric grounds. Assuming a square between four large particles (Fig. 3) the critical ratio of entrance of small particles [23] is:

$$d_v = (\sqrt{2} - 1) d_p = 0.414 d_p \Leftrightarrow \frac{d_L}{d_S} \approx \frac{d_p}{d_v} = 2.414 \quad (44a)$$

Assuming a triangle between three large particles (Fig. 3) the critical ratio of entrance [23] is:

$$d_v = \left(\frac{2}{\sqrt{3}} - 1 \right) d_p = 0.155 d_p \Leftrightarrow \frac{d_L}{d_S} \approx \frac{d_p}{d_v} = 6.414 \quad (44b)$$

During (mechanical) densification of particle mixtures the larger particles are somewhat mobile and therefore small particles may migrate through pores that are smaller at equilibrium. If large particles were added simultaneously with small particles the latter may get trapped (jammed) in the voids being unable to migrate. For undisturbed packing of large particles, a critical ratio of occupation may be defined. For the loose cubic (quadratic, Fig. 10) arrangement the pore diameter [23] is:

$$d_v = 0.732 d_p \Leftrightarrow \frac{d_L}{d_S} \approx \frac{d_p}{d_v} = 1.366 \quad (45a)$$

The tightest packing is achieved for two rhombohedral (Fig. 10) particle arrangements:

$$d_v = 0.414 d_p \Leftrightarrow \frac{d_L}{d_S} \approx \frac{d_p}{d_v} = 2.414 \quad (45b)$$

$$d_v = 0.225 d_p \Leftrightarrow \frac{d_L}{d_S} \approx \frac{d_p}{d_v} = 4.444 \quad (45c)$$

It is interesting that small particles (d_S) which just enter the square pore (Eq. (44a)) also just occupy the void of the tightest packing (Eq. (45b)) without disturbing the arrangement of large particles. It appears that packing ratios are rather independent on the absolute particle size and particle density, but mainly on the size ratio. Note that all critical size dependent ratios remain within the steep change of (inverted) volume fraction range ($d_L/d_S < 6.5$).

3.3. Trimodal particle packing

The influence of packing of different sized particles may be evaluated individually for each component by applying partial properties [25,26]. The maximum packing is modeled for coarse (C), medium (M), and fine (F) particles.

3.3.1. Partial properties

The total particle volume (cm^3) is expressed in terms of specific volumes ($v_p/\text{cm}^3/\text{g}$), Eq. (19) as:

$$V_p = m_1 v_1 + m_2 v_2 + m_3 v_3 \Leftrightarrow v_i = \left(\frac{\partial V_p}{\partial m_i} \right)_{v_j} \quad (46a)$$

or in terms of weight fractions (Eq. (20)) as:

$$v_p = \frac{V_p}{m_p} = w_1 v_1 + w_2 v_2 + w_3 v_3 \quad (46b)$$

Introducing $w_3 = 1 - w_1 - w_2$ we find that:

$$v_p = \frac{V_p}{m_p} = v_3 + w_1 (v_1 - v_3) + w_2 (v_2 - v_3) \quad (46c)$$

Partial differentiation with respect to w_1 yields [25,26]:

$$\begin{aligned} \left(\frac{\partial v_p}{\partial w_1} \right)_{w_2} &= \left(\frac{\partial v_3}{\partial w_1} \right) + (v_1 - v_3) + w_1 \left[\frac{\partial (v_1 - v_3)}{\partial w_1} \right] + w_2 \left[\frac{\partial (v_2 - v_3)}{\partial w_1} \right] = \\ &= (v_1 - v_3) + \left[w_1 \left(\frac{\partial v_1}{\partial w_1} \right) + w_2 \left(\frac{\partial v_2}{\partial w_1} \right) + w_3 \left(\frac{\partial v_3}{\partial w_1} \right) \right]_{w_2} = (v_1 - v_3) \end{aligned} \quad (47a)$$

Partial differentiation with respect to w_2 yields [25,26]:

$$\begin{aligned} \left(\frac{\partial v_p}{\partial w_2} \right)_{w_1} &= \left(\frac{\partial v_3}{\partial w_2} \right) + (v_2 - v_3) + w_1 \left[\frac{\partial (v_2 - v_3)}{\partial w_2} \right] + w_2 \left[\frac{\partial (v_2 - v_3)}{\partial w_2} \right] = \\ &= (v_2 - v_3) + \left[w_1 \left(\frac{\partial v_1}{\partial w_2} \right) + w_2 \left(\frac{\partial v_2}{\partial w_2} \right) + w_3 \left(\frac{\partial v_3}{\partial w_2} \right) \right]_{w_1} = (v_2 - v_3) \end{aligned} \quad (47b)$$

Rewriting Eq. (46c) yields [25,26]:

$$v_3 = v_p - w_1 (v_1 - v_3) - w_2 (v_2 - v_3) = v_p - w_1 \left(\frac{\partial v_p}{\partial w_1} \right)_{w_2} - w_2 \left(\frac{\partial v_p}{\partial w_2} \right)_{w_1} \quad (48a)$$

Rewriting Eq. (47a) yields [25,26]:

$$\begin{aligned} v_1 &= \left(\frac{\partial v_p}{\partial w_1} \right)_{w_2} + v_3 = v_p + (1 - w_1) \left(\frac{\partial v_p}{\partial w_1} \right)_{w_2} - w_2 \left(\frac{\partial v_p}{\partial w_2} \right)_{w_1} = \\ &= v_p + (1 - w_1)(v_1 - v_3) - w_2 (v_2 - v_3) \end{aligned} \quad (48b)$$

Rewriting Eq. (46b) yields [25,26]:

$$\begin{aligned} v_2 &= \left(\frac{\partial v_p}{\partial w_2} \right)_{w_1} + v_3 = v_p - w_1 \left(\frac{\partial v_p}{\partial w_1} \right)_{w_2} + (1 - w_2) \left(\frac{\partial v_p}{\partial w_2} \right)_{w_1} = \\ &= v_p - w_1 (v_1 - v_3) + (1 - w_2)(v_2 - v_3) \end{aligned} \quad (48c)$$

Partial differentiation of specific particle volume with respect to weight fraction of component 1 and component 2, respectively keeping the other weight fraction constant gives the slopes needed to calculate partial specific volumes of all components. Recalling Eq. (25):

$$1 - \phi_v = \phi_p = \varphi_1 \phi_1 + \varphi_2 \phi_2 + \varphi_3 \phi_3 = \phi_3 + \varphi_1 (\phi_1 - \phi_3) + \varphi_2 (\phi_2 - \phi_3) \quad (49)$$

Applying same procedure as before we may extract the partial volume fractions as:

$$\begin{aligned} \phi_1 &= \phi_p + (1 - \varphi_1) \left(\frac{\partial \phi_p}{\partial \varphi_1} \right)_{\varphi_2} - \varphi_2 \left(\frac{\partial \phi_p}{\partial \varphi_2} \right)_{\varphi_1} \\ &= \phi_p + (1 - \varphi_1)(\phi_1 - \phi_3) - \varphi_2 (\phi_2 - \phi_3) \end{aligned} \quad (50a)$$

$$\begin{aligned} \phi_2 &= \phi_p + \varphi_1 \left(\frac{\partial \phi_p}{\partial \varphi_1} \right)_{\varphi_2} + (1 - \varphi_2) \left(\frac{\partial \phi_p}{\partial \varphi_2} \right)_{\varphi_1} \\ &= \phi_p - \varphi_1 (\phi_1 - \phi_3) + (1 - \varphi_2)(\phi_2 - \phi_3) \end{aligned} \quad (50b)$$

$$\begin{aligned} \phi_3 &= \phi_p - \varphi_1 \left(\frac{\partial \phi_p}{\partial \varphi_1} \right)_{\varphi_2} - \varphi_2 \left(\frac{\partial \phi_p}{\partial \varphi_2} \right)_{\varphi_1} = \phi_p - \varphi_1 (\phi_1 - \phi_3) - \varphi_2 (\phi_2 - \phi_3) \end{aligned} \quad (50c)$$

The options to plot experimental results becomes challenging when the number of components is increased. In Fig. 20 the (inverse) volume fraction (ϕ_p, ϕ_p^{-1}) of mixtures of coarse and medium particles are plotted as a function of reduced volume fraction of medium (φ_M , top diagram) and of coarse particles (φ_C , bottom diagram) at different levels of constant fine φ_F . The diameter ratio is $d_C/d_M = 6.3$ and reduced volume fractions are related as ($\varphi_C + \varphi_M + \varphi_F = 1$).

In Fig. 21 the (inverse) volume fraction (ϕ_p, ϕ_p^{-1}) of mixtures of

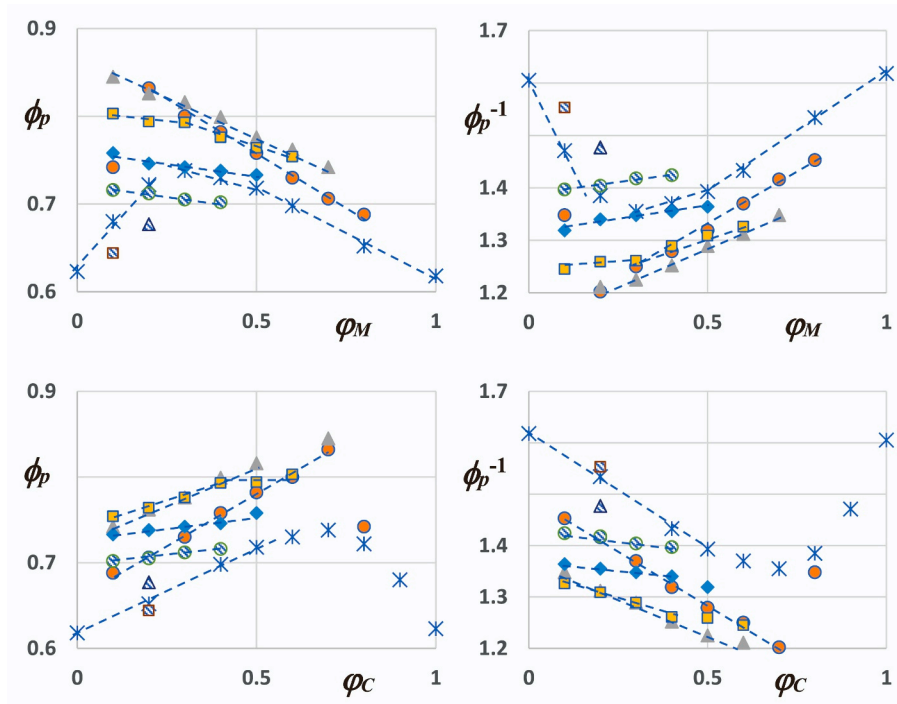


Fig. 20. Left diagrams: Volume fraction (ϕ_p) of course and medium sand particle mixture ($d_C/d_M = 6.3$) plotted as a function of reduced volume fraction of medium (ϕ_M , top diagram) and coarse (ϕ_C , bottom diagram) particles [19]. Right diagrams corresponding inverse volume fractions. Symbols: ϕ_F is kept constant at 0 (asterixis), 0.1 (circles), 0.2 (triangles), 0.3 (squares), 0.4 (diamonds), 0.5 (patterned circles), 0.6 (patterned triangles), 0.7 (patterned squares) ($\phi_F + \phi_C + \phi_M = 1$).

medium and fine particles are plotted as a function of reduced volume fraction of fine (ϕ_F , top diagram) and of medium particles (ϕ_M , bottom diagram) at different levels of constant coarse ϕ_C . The diameter ratio is $d_C/d_M = 8.0$ and reduced volume fractions are related as ($\phi_C + \phi_M + \phi_F = 1$).

In Fig. 22 the (inverse) volume fraction (ϕ_p, ϕ_p^{-1}) of mixtures of course and fine particles is plotted as a function of reduced volume fraction of fine (ϕ_F , top diagram) and of coarse particles (ϕ_M , bottom

diagram) at different levels of constant medium ϕ_M . The diameter ratio is $d_C/d_F = 50$ and reduced volume fractions are related as ($\phi_C + \phi_M + \phi_F = 1$).

In summary it appears that the content of fine particles is most important. In Fig. 21 the different constant levels of coarse particles and in Fig. 22 the different constant levels of medium size particles have very little influence on (inverse) volume fraction when $\phi_F > 0.3$. In those Figures the increase of constant fraction of ϕ_M and ϕ_C result only in

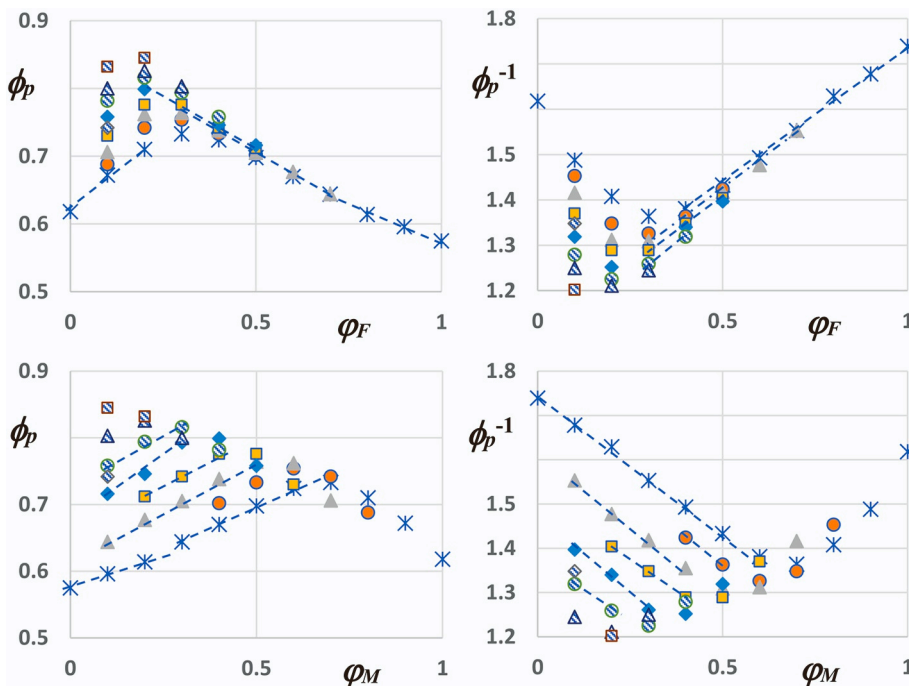


Fig. 21. Left diagrams: Volume fraction (ϕ_p) of fine and medium sand particle mixtures ($d_M/d_F = 8.0$) plotted as a function of reduced volume fraction of fine (ϕ_F , top diagram) and medium (ϕ_M , bottom diagram) particles [19]. Right diagrams corresponding inverse volume fractions. Symbols: ϕ_C is kept constant at 0 (asterixis), 0.1 (circles), 0.2 (triangles), 0.3 (squares), 0.4 (diamonds), 0.5 (patterned circles), 0.6 (patterned triangles), 0.7 (patterned squares), 0.8 (patterned diamonds) ($\phi_F + \phi_C + \phi_M = 1$).

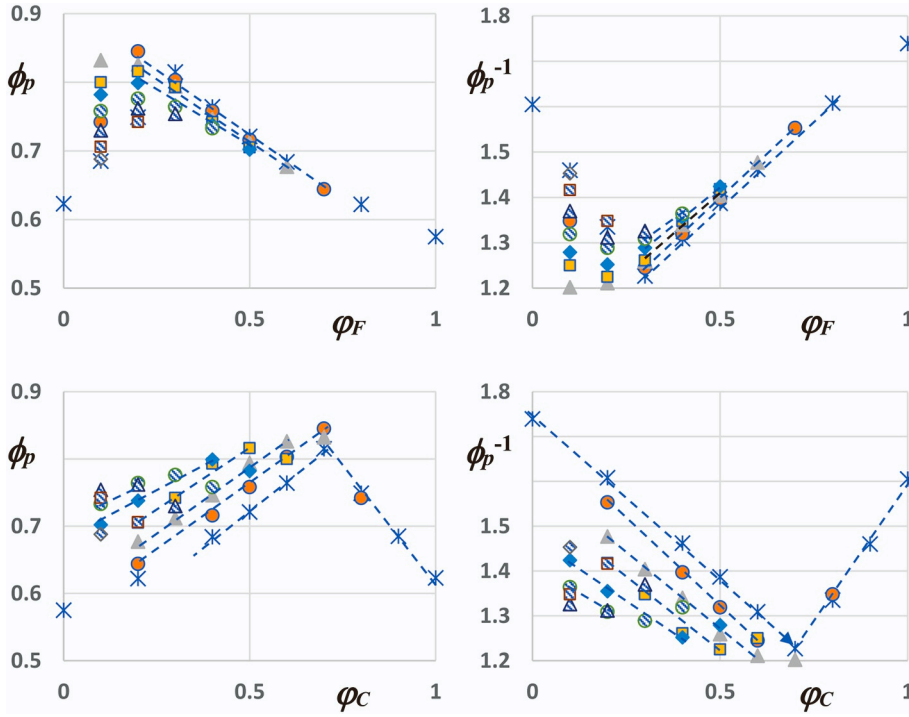


Fig. 22. Left diagrams: Volume fraction (ϕ_p) of fine and coarse sand particle mixture ($d_C/d_F = 50$) plotted as a function of reduced volume fraction of fine (ϕ_F , top diagram) and coarse (ϕ_C , bottom diagram) particles [13]. Right diagrams corresponding inverse volume fractions. Symbols: ϕ_M is kept constant at 0 (asterix), 0.1 (circles), 0.2 (triangles), 0.3 (squares), 0.4 (diamonds), 0.5 (patterned circles), 0.6 (patterned triangles), 0.7 (patterned squares), 0.8 (patterned diamonds) ($\phi_F + \phi_C + \phi_M = 1$).

parallel linear displacements when plotted as a function of low ϕ_C (ϕ_M constant) and low ϕ_M (ϕ_C constant). The interrelationships are more complicated in Fig. 20 when ϕ_F is kept constant. The parallel displacements of linear dependencies on ϕ_M and ϕ_M remain to some degree, but the number of linear segments seem to increase. The dependencies of volume fractions (ϕ_p) on composition appear generally just as linear as ϕ_p^{-1} , except for binary non-linear systems. Note that ϕ_p for three-component mixes exceeds rhombohedral packing $\phi_p = 0.704$ ($\phi_p^{-1} = 1.42$) for single particles (Table 6). Recalling Eq. (28):

$$1/\phi_p = \phi_p^{-1} = \varphi_1 \phi_{1,p}^{-1} + \varphi_2 \phi_{2,0}^{-1} + \varphi_3 \phi_3^{-1} = \phi_3^{-1} + \varphi_1 (\phi_1^{-1} - \phi_3^{-1}) + \varphi_2 (\phi_2^{-1} - \phi_3^{-1}) \quad (51)$$

Applying same procedure as before (Eqs. (50a)-(50c)) we may extract the partial volume fractions as:

$$\begin{aligned} \phi_1^{-1} &= \phi_p^{-1} + (1 - \varphi_1) \left(\frac{\partial \phi_p^{-1}}{\partial \varphi_1} \right)_{\varphi_2} - \varphi_2 \left(\frac{\partial \phi_p^{-1}}{\partial \varphi_2} \right)_{\varphi_1} \\ &= \phi_p^{-1} + (1 - \varphi_1) (\phi_1^{-1} - \phi_3^{-1}) - \varphi_2 (\phi_2^{-1} - \phi_3^{-1}) \end{aligned} \quad (52a)$$

$$\begin{aligned} \phi_2^{-1} &= \phi_p^{-1} + \varphi_1 \left(\frac{\partial \phi_p^{-1}}{\partial \varphi_1} \right)_{\varphi_2} + (1 - \varphi_2) \left(\frac{\partial \phi_p^{-1}}{\partial \varphi_2} \right)_{\varphi_1} \\ &= \phi_p^{-1} - \varphi_1 (\phi_1^{-1} - \phi_3^{-1}) + (1 - \varphi_2) (\phi_2^{-1} - \phi_3^{-1}) \end{aligned} \quad (52b)$$

$$\begin{aligned} \phi_3^{-1} &= \phi_p^{-1} - \varphi_1 \left(\frac{\partial \phi_p^{-1}}{\partial \varphi_1} \right)_{\varphi_2} - \varphi_2 \left(\frac{\partial \phi_p^{-1}}{\partial \varphi_2} \right)_{\varphi_1} \\ &= \phi_p^{-1} - \varphi_1 (\phi_1^{-1} - \phi_3^{-1}) - \varphi_2 (\phi_2^{-1} - \phi_3^{-1}) \end{aligned} \quad (52c)$$

The inverted (total) volume fraction of particles ($1/\phi_p = \phi_p^{-1}$) is plotted as a function of reduced volume fraction of medium (ϕ_M) and coarse (ϕ_C) particles keeping ϕ_F constant in Fig. 20. The inverted (total) volume fraction of particles ($1/\phi_p = \phi_p^{-1}$) is plotted as a function of reduced volume fraction of fine (ϕ_F) and medium (ϕ_M) particles keeping ϕ_C constant in Fig. 21. The inverted (total) volume fraction of particles ($1/\phi_p = \phi_p^{-1}$) is plotted as a function of reduced volume fraction of fine (ϕ_F) and coarse (ϕ_C) particles keeping ϕ_M constant in Fig. 22. The

reduced volume fractions are related as, $1 = \phi_F + \phi_M + \phi_C$.

For ideal mixing inverse volume fraction, a plane is drawn between coarse (C), medium (M) and fine (F) particle corners.

$$(\phi_p^{-1})^{id} = \varphi_C (\phi_C^*)^{-1} + \varphi_M (\phi_M^*)^{-1} + \varphi_F (\phi_F^*)^{-1} \quad (53)$$

where $(\phi_i^*)^{-1}$ are listed in Table 7. Alternatively, coarse particles are considered very large as compared to medium or fine particles and medium particles are very large as compared to fine particles. The ideal and particle mix models for three component system is illustrated in Fig. 23. At the corners the inverted volume fraction equals those of coarse ($(\phi_C^*)^{-1} = 1.605$ at $\varphi_C = 1$), medium ($(\phi_M^*)^{-1} = 1.618$ at $\varphi_M = 1$) and fine ($(\phi_F^*)^{-1} = 1.739$ at $\varphi_F = 1$).

The case when diameter ratios between small and large particles tend towards infinity is represented by shaded surfaces. Each side (binary

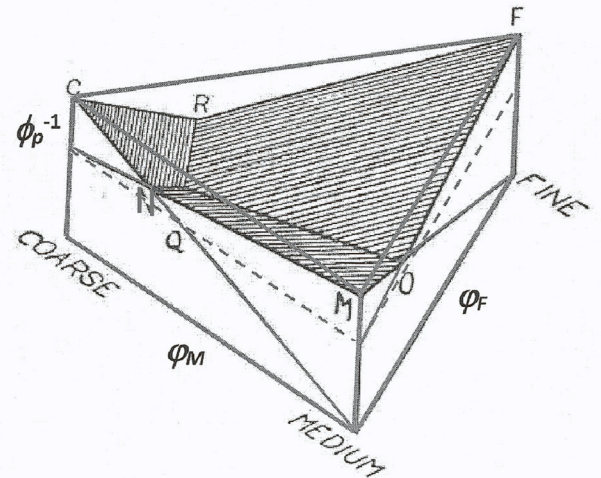


Fig. 23. Idealized packing model for a three (coarse, medium, fine) particle system with very large diameter ratios. The limiting values of $\phi_p^{-1} = 0$ and $\phi_p^{-1} = 1$ are indicated [15,19].

systems) of the triangular prism was characterized in Fig. 17 identifying the $\phi_p^{-1} = 0$ and $\phi_p^{-1} = 1$ model levels. The three planes can be obtained graphically and give the binary minimum (optimal packing) crossing points N , O and R . A line is drawn from O to $\phi_p^{-1} = 1$ at the coarse corner and from N to $\phi_p^{-1} = 0$ at the fine corner. Finally, a line is drawn from R to the intersection between previous lines. The intersection coincides with the crossing of a line drawn from R to the intersection between a line from C to $\phi_p^{-1} = 0$ at $\varphi_M = 1$ and the constant $\phi_p^{-1} = 1$ line (point Q). This defines the minimum (min = optimal packing) of the three-component particle system. The planar representation in Fig. 23 is quantified by the parallel displacements of and minima between linear segments (for each constant φ_i) in Figs. 20–22. Partial derivation of volume fractions to obtain three individual components (ϕ_i (φ_F , φ_M , φ_C)) for multiple lines within each plane illustrated in Fig. 23 is possible (Eqs. (52a),(52c), [25,26]), but would expand the analysis too much for present purposes.

3.3.2. Model for three-component particle mixing

Westman and Hugill provided analytical expressions for three-component particle mixtures [19]. If the three planes are labeled C , M and F in correspondence to the points through which they pass, then their equations are:

$$\phi_{p,C}^{-1} = \varphi_C (\phi_C^*)^{-1} \quad (54a)$$

$$\phi_{p,M}^{-1} = \varphi_C + \varphi_M (\phi_M^*)^{-1} \quad (54b)$$

$$\phi_{p,F}^{-1} = \varphi_C + \varphi_M + \varphi_F (\phi_F^*)^{-1} \quad (54c)$$

where $\phi_{p,C}^{-1}$, $\phi_{p,M}^{-1}$, $\phi_{p,F}^{-1}$ are the ordinates values on C , M and F planes, respectively. The minimum $\phi_{p,min}^{-1}$ value obtained at the junction of the three planes is given [19] by:

$$\phi_{p,min}^{-1} = \frac{\phi_C^{*-1} \phi_M^{*-1} \phi_F^{*-1}}{\phi_C^{*-1} \phi_M^{*-1} + \phi_M^{*-1} \phi_F^{*-1} + \phi_C^{*-1} \phi_F^{*-1} - (\phi_C^{*-1} + \phi_M^{*-1} + \phi_F^{*-1}) + 1} \quad (55a)$$

where ϕ_i^{*-1} is a short-hand expression for $(\phi_i^*)^{-1}$. If the course, medium and fine particles themselves have the same ϕ_p^{-1} value, then $\phi_{p,C}^{-1} = \phi_{p,M}^{-1} = \phi_{p,F}^{-1}$ and the minimum inversed volume fraction is given [19] by:

$$\phi_{p,min}^{-1} = \frac{(\phi_C^{*-1})^3}{(1 - \phi_C^{*-1})^3 + (\phi_C^{*-1})^3} = \frac{[(\phi_C^*)^{-1}]^3}{[1 - (\phi_C^*)^{-1}]^3 + [(\phi_C^*)^{-1}]^3} \quad (55b)$$

For $(\phi_C^*)^{-1} = 1.605$ it was found that $\phi_{p,min}^{-1} = 1.057$ [19]. This value may be obtained by mixing course, medium and fine particles in the proportion $\varphi_C = 0.66$, $\varphi_M = 0.25$ and $\varphi_F = 0.09$. This nearly corresponds to the experimentally observed minimum, $\phi_{p,min}^{-1} = 1.202$ at $\varphi_C = 0.7$, $\varphi_M = 0.2$ and $\varphi_F = 0.1$. The experimental location of minimum $\phi_{p,min}^{-1} = 1.183$ is, however found at $\varphi_C = 0.7$, $\varphi_M = 0.1$ and $\varphi_F = 0.2$. Although predicted $\phi_{p,min}^{-1}$ is somewhat off experimentally found value it is quite remarkable that it was derived based on $(\phi_C^*)^{-1}$ alone. In Figs. 20–22 ϕ_p appeared equally linearly dependent on φ_C , φ_M and φ_F as ϕ_p^{-1} . Therefore $\phi_C^* = 0.623$ was inserted into Eq. (55b). Then $\phi_{p,max} = 0.819$, which is just as close to experimentally found $\phi_{p,max} = 0.845$ at $\varphi_C = 0.7$, $\varphi_M = 0.1$ and $\varphi_F = 0.2$ as model predicted $\phi_{p,min}^{-1}$. The model packing density (particle volume fraction) exceeds the densest rhombohedral single particle packing ($\phi_p = 0.7405$, Table 6), but it is in the range of maximum model packing densities ($\phi_{p,max} = 0.856$ for coarse-medium, $\phi_{p,max} = 0.838$ for medium-fine and $\phi_{p,max} = 0.840$ for coarse-fine) for two-component mixtures. Again, the three-component packing was predicted using only volume fraction of single coarse system.

3.4. Summary

The maximum packing density of monomodal, bimodal and trimodal spherical particle mixtures were evaluated. Bimodal particle systems were characterized by partial volumes, partial volume fractions and by partial inverse volume fractions. Additionally, models were introduced which predicted the enhanced packing in terms of volume fractions and inverted volume fractions based on monomodal volume fractions and inverse volume fractions of large and small particles, respectively. Mixing and excess functions were introduced to quantify the change from ideal mixing properties. Experimentally it was observed that both particle size ratio (d_L/d_S) and mixture composition (reduced volume fraction of small (φ_F), medium (φ_M) or large (φ_C) particles) have significant influence on volume fraction. Fig. 24 illustrates the mutual dependence of volume fraction on particle size ratio (d_L/d_S) and on reduced volume fraction of small particles (φ_S).

Binary particle mixtures characterized by $1.0 < d_L/d_S < 1.4$ are commonly used for modeling purposes to avoid crystallization phenomena (cluster formation). However, for larger size ratios these mixtures were found to reach higher volume fractions than single particle beds. In Fig. 19 ϕ_p increased as a function of d_L/d_S with a break (critical) point at $6.5 < d_L/d_S < 7.0$ after which the dependence levels off towards a final saturation value (ϕ_{sat}). The break point corresponds to triangular pores between three larger particles ($d_L/d_S = 6.414$, Eq. (44b)). The limiting condition for dense packing is that voids between large particles are sufficient for small particles to migrate to equilibrium positions. It appears that packing ratios are rather independent on the absolute particle size and its density, but mainly on the size ratio. For high d_L/d_S the volume fraction may reach $\phi_p = 0.85$.

The volume fraction (ϕ_p) increases also with φ_S , reaches a maximum (ϕ_{max}) at $0.25 < \varphi_S < 0.45$ after which it is reduced to a value corresponding to random close packing ($0.63 < \phi_{RCP} < 0.64$) or random loose packing ($0.59 < \phi_{RCP} < 0.60$). It was, however experimentally shown that $\phi_p < \phi_{RCP} < \phi_{RCP}$ at $\varphi_F = 0$ (ϕ_L^*) and at $\varphi_F = 1$ (ϕ_S^*). The volume fraction of models and particles were: $\phi_C^* = 0.623$, $\phi_M^* = 0.618$ and $\phi_F^* = 0.575$ (Table 7). Fig. 25 illustrates the change in packing when d_L/d_S is varied as 2.5, 5 and 9 at $\varphi_S = 0.2$ and $\varphi_S = 0.8$.

The presence of large particles affects only locally the random packing of small ones on its surface (excluded volume). The upper row illustrates packing when φ_F is low (0.2) and small particles fill the voids between large particles. When d_L/d_S are reduced (fraction of large particles become larger) small particles get jammed between large ones. As a result, the packing of large particles is disrupted by small ones. A random jammed close packing reach maximum at $0.63 < \phi_{RCP} < 0.64$.

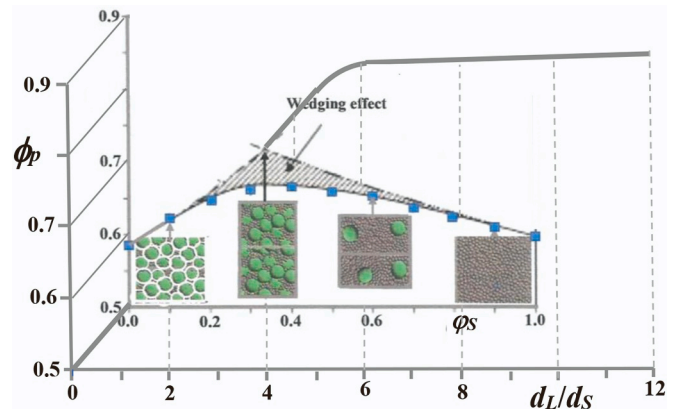


Fig. 24. Particle volume fraction (ϕ_p) plotted as a function of particle size ratio (d_L/d_S , Fig. 19) and of reduced volume fraction of small particles (φ_S). Insert diagram at constant $d_L/d_S = 4$ (Identified by ϕ_{max} , Fig. 16): Left branch, binary systems of small φ_S (Eq. (34b)). Right branch, binary system of large φ_S (Eq. (34a)).

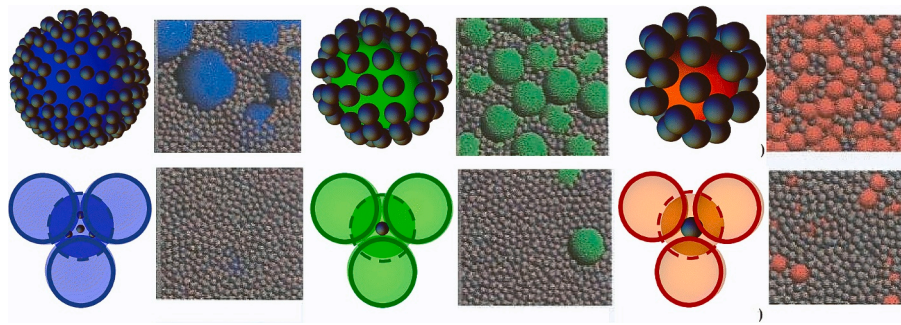


Fig. 25. Schematic illustration of the influence size ratio ($d_L/d_S = 9$ (left), $d_L/d_S = 5$ (middle) and $d_L/d_S = 2.5$ (right)) on small particles around large ones (upper row, $\varphi_F = 0.2$) and on pore size formed between large molecules (lower row, $\varphi_F = 0.8$) [22].

The lowest volume fraction of a mechanically stable particle assembly is represented by random loose packing $0.59 < \phi_{RLP} < 0.60$. Both bimodal and trimodal packing models are based on monomodal packing densities when the reduced volume fraction of them is high. Denotations for different deficient packings are illustrated in Fig. 26.

Three-modal mixing was represented by three planes (Fig. 23) which deviate considerably from the single plane representing ideal mixing. The three planes can be obtained graphically by extrapolation from corresponding binary systems. The crossing of each two planes represents linear optimal bimodal packings (ϕ_{min}^{-1}) and the crossing point of all three planes the ultimate minimum of trimodal packing. A simple model is presented by which the ultimate packing minimum and its coordinates can be successfully estimated.

4. Experimental challenges

In first section the aim was to identify methods to determine the diameter of equivalent spheres characterizing average particle properties for single particles and particle size classes as well as for particle size segments of powders. In second section the dependence of packing density expressed as (partial) specific volumes, volume fractions and inverse volume fractions (apparent volumes) on reduced particle volume fractions in binary and ternary systems were evaluated. Reference models to determine maximum packing based on (inverted) volume fractions ($\phi_{p,max}$, $\phi_{p,min}^{-1}$) were introduced. The packing of bimodal and trimodal particle mixtures was achieved by careful and thorough mixing. In this section the influence of experimental procedures to maintain homogeneity of particle mixtures is shortly evaluated. Segregation of different particle size classes may occur spontaneously, which makes sampling and mixing very difficult. Segregation leads to clustering

(wedge effects) and to excluded volume contributions, where small particles assemble around large particles due to loss of mobility freedom. Particles may also form local clusters through percolation which seriously distort original packing structures.

4.1. Particle assembly at macroscopic interfaces – excluded void fraction

At large interfaces small particles lose one dimension of mobility freedom which results in spontaneous assembly as particle layers at interfaces (Fig. 27).

The void fraction is least at macroscopic test compartment planes as compared to curved walls (test cylinders). At the corners of a quadratic container the void fraction is greatest. For a minimum void fraction cylindrical test compartments are to prefer. Wall effects at test cylinder surfaces should be considered when particle size is large ($d_p > 5$ mm). It can be of 10–15% magnitude for 10–12 mm particles in a 100 mm test cylinder. The results are valid only for comparable test cylinders.

4.2. Particle layering

As shown in Table 6 monomodal packing formations of close-packed spheres consist of four basic types of unit cells. The packing density (ρ_c) can be calculated by dividing the volume of spheres ($4\pi r^3/3$) by the unit cell volume of each formation. The resulting packing densities are; $\rho_c = \pi/6$ (cubes), $\rho_c = \pi/3(3)^{1/2}$ (orthorhombic), $\rho_c = 2\pi/9$ (tetragonal) and $\rho_c = \pi/3(2)^{1/2}$ (rhombohedral). The volume fraction is improved for an increased number of layers only for $N_C = 10$ and $N_C = 12$ packings (Fig. 28).

Note that volume fractions of model $N_C = 10$ and $N_C = 12$ (two highest lines) model packings exceed for small N_i tetragonal ($\phi_p = 0.6981$, $N_C = 10$) and rhombohedral ($\phi_p = 0.7405$, $N_C = 12$) packing densities for single particle beds (Table 6, Fig. 19).

Two, four, eight and twenty flat layers of 0.5–1.0 mm sand and 9.0 mm bearing balls of stainless steel were introduced into a test cylinder. It was found that particles could reasonably easily be mixed to a homogeneous mixture. Fig. 29 illustrates the dependence of inverse volume fraction and its deviation ($\delta = 2/N_p$) of 70% coarse particle mixture on inverse number of initial layers ($1/N_i$).

Linear extrapolation yields $\phi_p^{-1} = 1.27$ which is very close to the predicted value $\phi_p^{-1} = 1.285$. The shrinkage ($\delta = 2/N_p$) is thus initially a linear function of $1/N_i$ (up to 20 layers). A difference between experimental and deviation (δ) occurs, since a small demixed zone between the layers could not be avoided. This is thus a direct proof of degree of dispersion during mixing.

4.3. Particle packing in test cylinders

McGeary investigated the packing efficiency of particles in test cylinders of different diameter by forming particle layers [23]. He observed that neither particle density or size influenced significantly the final

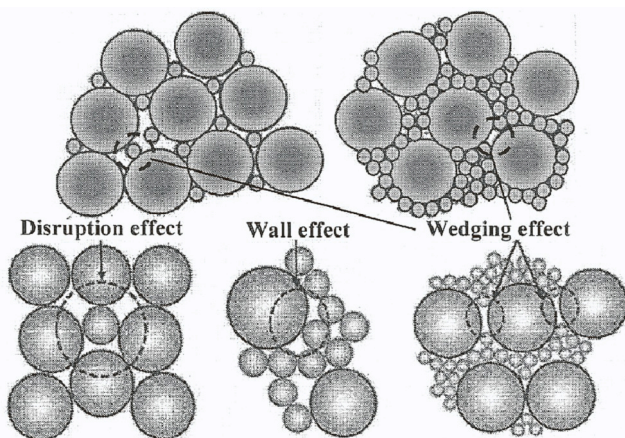


Fig. 26. Common denotation of packing deficiencies, disruption (loosening) effect, wall (excluded volume) effect and wedging effect.

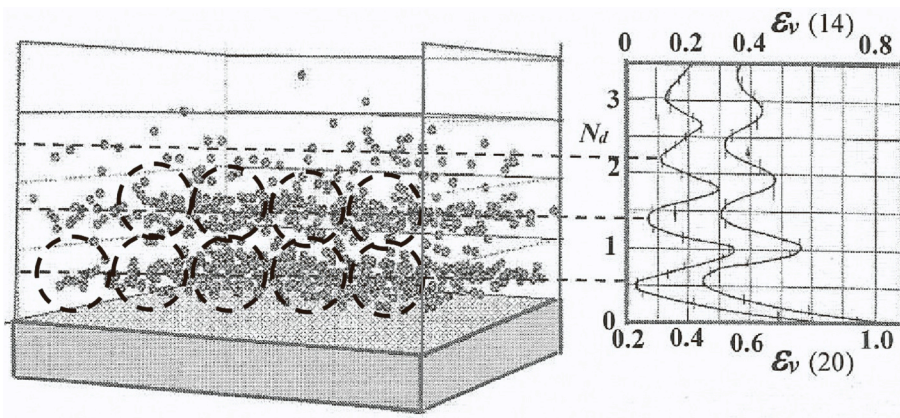


Fig. 27. Left diagram: Schematic presentation of small particle assembly at large surfaces. Void fraction ($\epsilon_v = 1 - \phi_p$) is lowest at the center of particle layers. Right diagram [27]: Dependence of void fraction (ϵ_v) on the distance from surface expressed as number of large particle diameters (N_d). Assuming contact between large particles and surface (dotted circles), the void fraction is smallest at the center of particles (radial distances, $r_p = d_p/2$). Left curve and bottom void fraction scale, radial distribution for cylinder diameter/particle size ratio = 20.3. Right curve and top void fraction scale, radial distribution for cylinder diameter/particle size ratio = 14.1.

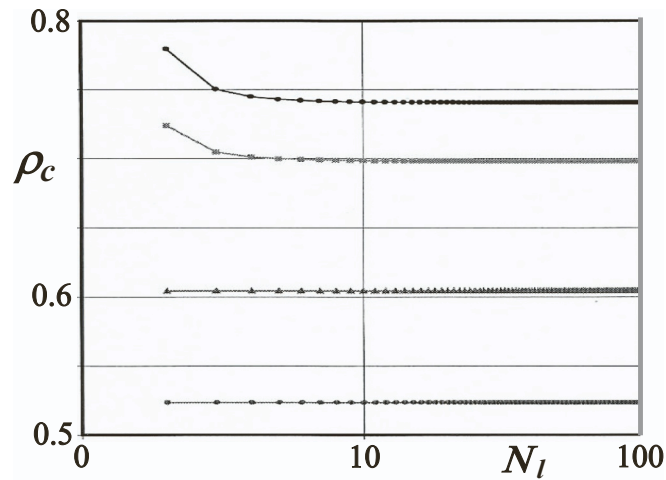


Fig. 28. Change in packing density (ρ_c) of single spherical particles when the number of layers (N_l) increases. Top line represents $N_c = 12$, next $N_c = 10$, next $N_c = 8$ and lowest $N_c = 6$ packing, where coordination number N_c identifies number of nearest neighbors [28].

volume fraction. However, both the size and shape of test container influence the type and density of particle packing. In general, cylindrical containers caused almost complete orthorhombic pattern. Simple cubic (quadratic) arrangements were found to be unstable and was not observed experimentally. Moreover, rhombohedral packing did not occur in mechanical packing because the used vertical compression force enforced rhombohedral arrangements. The dependence of (inverse) volume fraction (ϕ_p, ϕ_p^{-1}) on test cylinder diameter (D_c) to particle diameter (d_p) is shown in Fig. 30.

When monodispersed spheres were fitted into test cylinders of increasing diameter the packing first decreased, but started to increase as 2, 3 or 4 spheres formed a layer (only integral numbers are considered). Seven spheres produced the familiar hexagonal layer pattern which is associated with efficient packing. A ring was formed around a center of three spheres for 9, 10 and 12 spheres in a layer. At 14 spheres per layer, the orthorhombic ring pattern appears were particles formed a ring around a center of four spheres. These filled rings did not, however cause a tight or locked (jammed) arrangement. At $D_c/d_p = 200$ there were about 33,000 particles per layer and then $\phi_p = 0.625$ which agreed very closely with experimental values. In summary, a maximum experimental packing density can be obtained only if the test cylinder diameter is at least an order of magnitude larger than particle diameter.

4.4. Particle asymmetry

Wadell's sphericity of irregular particles (Eq. (10a)) was specified as the ratio of surface area of a sphere with the same volume as the particle to the actual surface area of the particle [10,11]. For spherical particles the sphericity was defined as:

$$\psi = \frac{\sqrt[3]{36\pi V_p^2}}{A_p} = 4.836 \left(\frac{V_p^{2/3}}{A_p} \right) \quad (56)$$

For spheres $\psi = 1$. Sphericity is sometimes referred to as shape factor and then its inverse is denoted the area-volume shape factor ($1/\psi$). Porosity of randomly packed irregular particle beds is closely related to sphericity. In Fig. 31 the volume fraction of randomly packed uniform-sized particle beds are plotted as a function of their sphericity (ψ).

Sphericity may be averaged over the number of particles contained in the bed and hence be used for characterizing average particle shapes. Particle asymmetry has, indeed a profound influence on packing density (ϕ_p). As particle diameter decreases surface forces resulting in adhesion

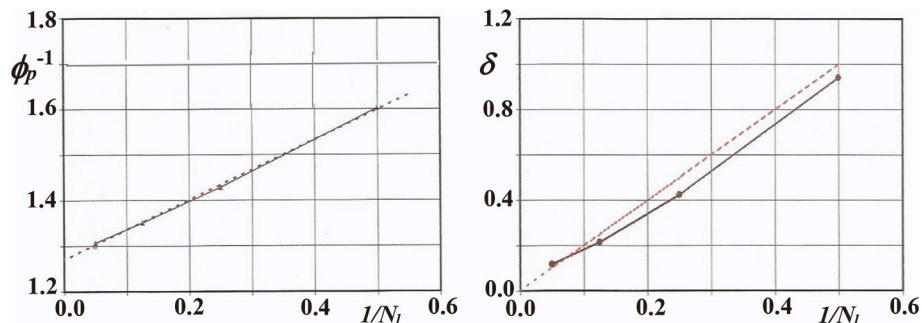


Fig. 29. Inverse volume fraction ($1/\phi_p = \phi_p^{-1}$) and deviation ($\delta = 2/N_p$) of a 70% mix of coarse 9.0/(0.5–1.0) size particle mix plotted as a function of inverse number of initial layers ($1/N_l$). Solid line experimental results, dotted line = model fit [28].

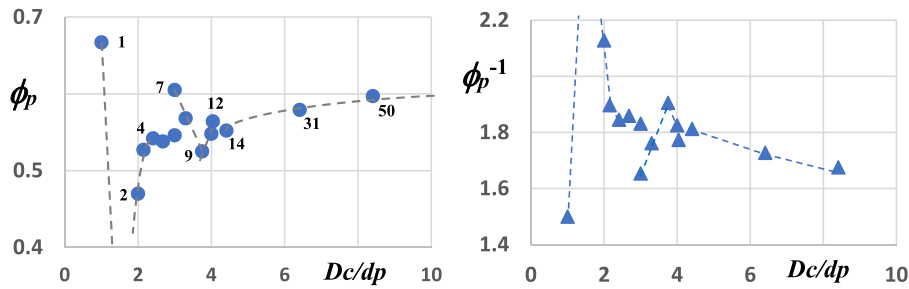


Fig. 30. Dependence of volume fraction (circles, left diagram) and inverse volume fraction (triangles, right diagram) on diameter ratio of test cylinder and particle diameter ratio (D_c/d_p). Inserted numbers = particles per layer [23].

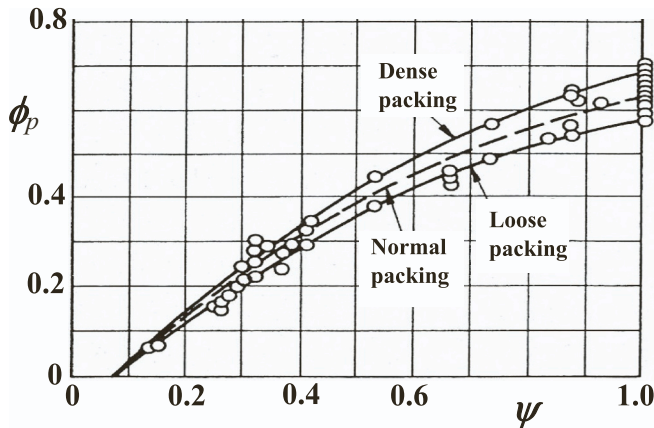


Fig. 31. Volume fraction (ϕ_p) of randomly packed uniform-sized particle beds plotted as a function of their sphericity (ψ). Dense (top line), normal (dashed middle line) and loose (bottom line) packings are indicated [29].

increase, since A_p/V_p ratio is enhanced (Table 2). Deformation of particles results in bridging, arching and percolation.

4.5. Particle percolation and segregation

Asymmetric particles self-assemble in structures which deviate from ideal packing of hard spheres. When the size ratio (d_L/d_S) of binary and ternary mixtures is large enough small particles may enter and pass through these voids. When size ratio is higher than $d_L/d_S > [3 + 2(3)^{1/2}] = 6.46$ (Fig. 19), small particles naturally segregate (flow through pores in particle bed) forming a separate phase at the bottom due to gravity, while large particles are still mixed with the rest of small particles. Segregation of small particles through pores occurs when additional mechanical impacts (tapping, vibration) are introduced. Particle mixtures are rarely homogeneous which leads to cluster formation (percolation) and particle segregation. For disordered packing this threshold is significantly smaller. Flow of small molecules through particle beds happens even for smaller d_L/d_S , because the random structure leads to larger pores than expected. For this reason, one can observe small particle segregation also for $d_L/d_S < 5$.

Deformed particles form preferential undefined “bonds” at their edges. Bond percolation theory describes the behavior of assembled networks when the number of “nodes” or “links” increases. This is a geometric type of particle phase transition, since at a critical fraction of small clusters they merge into significantly larger connected spanning clusters (gels). The edges or bonds between each two neighbors (coordination number, $N_C = 2$) may be open allowing small particles to pass freely (f) through the network with probability p_f or blocked (no passages) with probability $1-p_f$. The focus is on whether small particles can penetrate through the percolated network or not. Site percolation

considers whether sites are occupied (probability p_o) or empty with probability $1-p_o$. In addition to the question whether small particles can pass the network or not, the interest is on what fraction of bonds will be disconnected. The system may be normalized by a critical probability p_c , below which probability is always zero and above which probability is always unity. In practice, this criticality is easy to observe. Even for small number of particles the probability of an open path network increases sharply from very close to zero to unity in a short span of p_o -values.

For most infinite networks p_c cannot be calculated exactly. However, for two-dimensional square (2D, $N_D = 2$) lattices the bond percolation is $p_c = 0.5$. For multiple dimensions the critical threshold is $p_c = 1/(N_C - 1)$ [30]. For site percolation the p_c value is not known from analytic derivation, but only via simulations of large lattices [31]. Large networks of high or low degree of clustering are modeled by various functional dependencies. For a given degree of network distribution, the clustering leads to a larger threshold. For a fixed number of links, the clustering structure reinforces the core network. As a result, the global connections are diminished.

For probabilities below critical value ($p_f < p_c$) phases are denoted subcritical. Then the probability that a specific point (the origin) with a diameter d_p is contained in an open cluster with a maximal number of open bonds, decays to zero exponentially in d_p . In two dimensions it converges to $p_c = 0.5$. Then there is a unique infinite closed cluster with maximal number of closed bonds. The subcritical phase may therefore be described as finite open associates in an infinite open medium. It follows that in two dimensions, the supercritical phase is dual to a subcritical percolation process. For supercritical phases ($p_f > p_c > 0.5$) there is finite closed clusters in a infinite open medium. In three and more dimensions ($N_D > 3$) there is coexistence of infinite open and closed clusters for $p_c < p_f < (1 - p_c)$. Percolation has a singularity at $p_f = p_c$ and many properties behave as of a power law with $p_f - p_c$ at p_c . Scaling theory predicts the existence of critical exponents which depend on N_D determining the class of singularity.

4.6. Particle clusters – fractal dimensions

Clusters may be characterized by fractal dimensions (f_D). The mass of cluster (m_c or molar mass M_c) scales to its spatial size (d) as $m_c = d^{f_D}$. When $f_D = 1$ the cluster represents a chain structure, when $f_D = 2$ the cluster is planar and when $f_D = 3$ the cluster is three-dimensional. For hard sphere clusters the scaling exponent s_f is related to fractal dimension [32] as:

$$s_f = \frac{N_D}{f_D + 2} \tag{57a}$$

where N_D denotes space dimension. When the excluded volume effect is screened out near the percolation point, the scaling exponent decreases [32] as:

$$s_f = \frac{N_D(N_D + 2 - 2f_D)}{2(N_D + 2 - f_D)} \quad (57b)$$

For a set of particles distributed in space, the fractal dimension can be defined according to $m_C = d^{f_D}$ in a similar manner. In Fig. 32 fractal dimensions are derived from measurements of logarithmic normalized perimeter as a function of linear or logarithmic step length (λ).

Two-dimensional fractals may be determined with atomic force or visual light microscopy. Three-dimensional fractals may be characterized by scattering methods where wavelength serves as step length. The relative distance from the critical point is given [32] by:

$$l_f = \frac{p_f - p_c}{p_c} \quad (58)$$

where p_f and p_c refer to probability that any particular bond is formed and to the threshold point where all bonds are formed. The average mass of the cluster m_C (or molecular weight M_C) and its correlation (cluster) length (l_C) are given [32] by:

$$m_C = l_f^{-1.76} \quad (59a)$$

$$l_C = l_f^{-0.88} \quad (59b)$$

Fractal dimensions characterize the distribution function of percolation models. For clusters of low fractal dimension the mass grows slower in diameter (density decreases) than for another cluster having large fractal dimension. Clusters having low fractal dimension have obviously a more open porous structure as compared to clusters having the same diameter.

4.7. Cluster energy – Flory-Huggins lattice model

Chain structure clusters are common for gels. At a critical fraction of small clusters and experimental conditions they merge into significantly larger connected spanning clusters. Since the mass of clusters (m_C) scales to its spatial size (d) as $m_C = d^{f_D}$ gels were characterized by fractals (f_D) [33]. Flory-Huggins lattice model may be used to quantify cluster formation in condensed media. Solvent molecules and each segment of cluster chains are assumed to have equal volumes as lattice cell units. The interaction is disregarded when deriving the mixing term. For such

athermal ideal solutions the internal energy, the enthalpy and the volume of mixing is zero. The ratio between the volumes of the particle cluster to that of the solvent represents the degree of clustering (number of cluster segments, $N_c \approx V_C^*/V_L^*$). Since the cluster volume is $V_C^* \approx N_c V_L^*$ the volume fractions may be expressed as [33,34]:

$$\phi_L = \frac{x_L V_L^*}{x_L V_L^* + x_C V_C^*} = \frac{x_L}{x_L + x_C N_c} = \frac{n_L}{n_L + n_C N_c} \quad (60a)$$

$$\phi_C = \frac{x_C V_C^*}{x_L V_L^* + x_C V_C^*} = \frac{x_C N_c}{x_L + x_C N_c} = \frac{n_C N_c}{n_L + n_C N_c} \quad (60b)$$

Molar cluster volume is $V_C^* = M_C/\rho_C$, cluster amount is $n_C = m_C/M_C$ and cluster mole fraction is $x_C = n_C/(n_L + n_C)$. With these pre-set conditions, the molar combinatorial (C) Gibbs free energy of mixing is represented purely by the combinatorial entropy of mixing [33,35]:

$$G_m^C \approx -TS_m^C = RT(x_L \ln \phi_L + x_C \ln \phi_C) \quad (61)$$

The chemical potentials of mixing are obtained by partial differentiation [33,35]:

$$G_L^C = \mu_L^C = RT \left[\ln \phi_L + \phi_C \left(\frac{N_c - 1}{N_c} \right) \right] \quad (62a)$$

$$G_C^C = \mu_C^C = RT [\ln \phi_C - \phi_L (N_c - 1)] \quad (62b)$$

Flory-Huggins model can be related to previous particle packing models by replacing the number of small dispersive liquid molecules or rather empty lattice units by number of voids. The cluster is assumed to represent an assembly of single particles ($V_C^* \approx N_c V_p^* \approx N_c V_c$). The success of Flory-Huggins model in predicting particle clusters is obviously based on the assumption that $V_L^* \approx V_p^* \approx V_c$ (V_c = lattice cell volume). The expressions for particle clusters do not apply for low degree of clustering (small N_c). In presence of mutual cluster-liquid interaction it may be considered by introducing an enthalpic term [33,35] enabling estimation of cluster solubility (phase transitions) in solvents.

4.8. Time dependence

It has been shown that a slow compaction dynamics of particle beds can be described [22] by:

$$\phi_p(t) = \phi_f - \frac{\phi_f - \phi_i}{1 + \ln(1 + \tau)} \quad (63)$$

where f = final and i = initial values, $\tau = t/N_m$ normalized time, t = time and N_m = number of mechanical impacts (taps, vibrations, compressions) causing compaction. The logarithmic scale expressing time dependence emphasize the slow (glassy like) dynamic behavior. It has been shown that N_m is a relevant flowability indicator in that a large value corresponds to low flowability. It is exponentially proportional to the ratio of energy barrier for the escape of small particles from pore sites to the energy injected per mechanical impact [22]. A high ratio corresponds to particle jamming and a small ratio to high particle mobility.

4.9. Summary

Due to loss of mobility freedom at large walls small particles assemble in layers which creates fluctuating excluded voids (volumes) as a function of the distance from the wall. Porosity is least for particles at planes as compared to curved surfaces and corners. This result in dependence of packing on the container shape. Both the size and shape of test container was, indeed found to influence the type and density of particle packing.

Packing density of cubic and of orthorhombic order remains constant as the number of layers increase. Packing density of tetragonal and rhombohedral order decrease, however, when more particle layers were

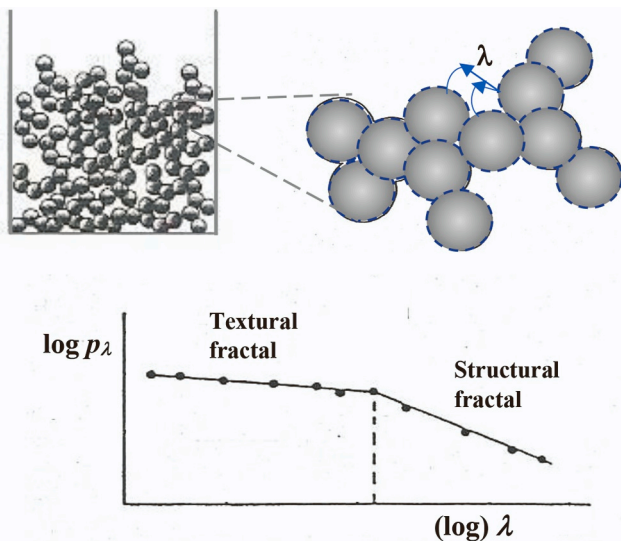


Fig. 32. Fractal dimension of a gel cluster is determined by measuring the slope of logarithmic normalized perimeter plotted as a function of linear or logarithmic step length (λ). Both the structural fractal of the cluster (large λ) and the textural fractal of the unit particles (small λ) can be distinguished as changed slopes.

added.

Average particle shape was characterized by sphericity (3D) and circularity (2D). Packing expressed as volume fraction increases rather smoothly as a function of enhanced sphericity. Simultaneously a modest dependence on packing density increases.

Particle asymmetry induces preferential aggregation due to bridging, arching and percolation which influences segregation of different particle size classes. Models based on bond and site percolation characterize probabilities for loose and dense cluster formation and for particle segregation.

Fractal dimensions characterize the distribution function of percolation models. Textural and structural fractals may be used to characterize particle clusters in one-to-three dimensional open and closed structures based on probabilities for bond formation. For clusters of low fractal dimension the mass grows slower in diameter (density decreases) than for another cluster having large fractal dimension. Clusters having low fractal dimension have obviously a more open porous structure as compared to clusters having the same diameter.

Cluster formation energy may be established by modifying Flory-Huggins lattice model for polymer solutions. It is based on athermal entropy of packing solvent molecules (replaced by voids) and cluster units in equally sized lattice cells. The negative molar combinatory entropy is assumed to equal molar combinatory Gibbs free energy of mixing non-interactive hard spheres.

Time dependence of powder compaction is related to ratio of change in volume fraction to logarithm of compaction time normalized by number of mechanical impacts. It is related to the energy barrier for the escape of small particle from pore sites between large particles.

The enhanced mobility of small particles within large particle matrices has some interesting features (cf. Fig. 2). As shown in Fig. 33 colloidal particles ($1 \mu\text{m} < d_p < 10 \text{ nm}$) may, due to their increased thermal mobility be used to fluidize dry coarse powders.

Particles with $d_p > 1 \mu\text{m}$ are not so useful, since their large number of active sites (unsaturated broken bonds) enhances cohesion (formation of percolation clusters) which reduces their mobility. Larger particle powders have less cohesion and larger fluidity but are restricted by unfavorable size ratios (d_L/d_S). Due to the very large surface to volume ratio (a_p/v_p , Table 2) the need for space or polar liquids to neutralize bond formations is very large.

5. Conclusions

Particles may be divided into different size ranges (classes) which alone and added to powders exhibit particular properties. The

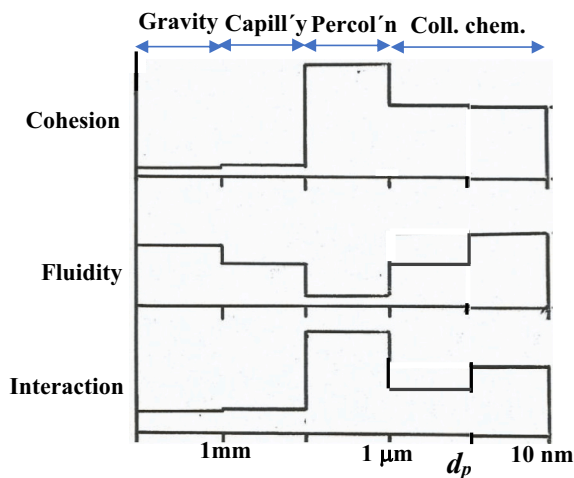


Fig. 33. Schematic illustration of the influence of small particles on the properties of dry large particle powders (colloid particle classes in the $10 \mu\text{m} - 10 \text{ nm}$ range). The dominant forces are indicated.

exceptional properties of colloid (10–100 nm) and nano (1–10 nm) particles may be related to their extremely small mass (reduced influence of gravity) and large surface area-to-volume ratio.

Particle shapes may be averaged by sphericity (3D) and by circularity (projected 2D). For multi-modal powders two of experimentally determined properties characterizing corresponding equivalent spheres provide comparable average sizes for each particle size class. Average (median, mean, mode) sizes can be extracted from size distributions of multimodal powders.

Mono-, di- and trimodal particle packing efficiency is expressed as volume fractions and inverted volume fractions of close-packed hard spheres and related to standard cubic, orthorhombic, tetragonal and rhombohedral packing properties. Simple models are presented which reveal the relative influence of fine, medium and coarse particles as a function of their respective amount and size ratios.

Experimental challenges relate to the influence of measuring test compartment shape on particle layering and of particle shape on packing density (volume fraction). Particle asymmetry induces preferential aggregation through bond and site percolation resulting in dense closed or loose open structures. Asymmetry induces small particle jamming or particle segregation. The cluster structure may be characterized by structural fractals of the gel and textural fractals identifying the particles involved. A modified Flory-Huggins lattice model enables determination of ideal combinatory entropy for the cluster assembly. A model is presented which relates time dependent volume fraction to logarithmic time dependence of compaction.

Symbols and indices

A	surface area
E	(information) entropy
G	Gibbs (free) energy
H	Hamaker constant
M	molar mass, moment
N	Number
R	gas constant
S	entropy
T	(absolute) temperature
V	volume

Upper index

Δ	difference
Σ	sum
δ	deviation
ϵ	porosity, pore fraction
μ	chemical potential
λ	(fractal) step length
ρ	density
σ	surface energy, standard deviation
τ	normalized time
ϕ	volume fraction
φ	reduced volume fraction
ψ	sphericity
ω	circularity
C	combinatory
D	dispersive
E	excess
L	linear
M	mixing
N	nonlinear
R	residual
b	bulk
exp	experimental
id	ideal
mix	mixing

s surface, size
 •, * neat pure

Symbols and indices

a molecular/monomer area
d diameter
e elongation
f frequency, function, fractal dimension
g G/N or g/v
h height
k coefficient
l length, later, distance
m mass
n amount, number of moles
p perimeter, probability
r radius
s size, scaling exponent
t time
v fraction of volume
 ν specific or partial volume
w width, weigh fraction
x mol fraction

Lower index

A Avogadro
C coarse, coordination, cluster
D (space) dimension, diameter
F Feret's, fine
G geometric
L length, liquid, large
M Martin's, moment, medium
N number, normal, N^{th} unit, nonlinear
S small, solid
V volume
a area, apparent
c cube, cluster segment, cell, critical
d diameter
dh dodekahedron
f free, formed, final
fo formation
h hydrodynamic
i component, segment, initial
ih icosahedron
l longest, layers
m molar, medium, mechanical
max maximum
min minimum
o occupied
p particle
r radius
s shortest
sat saturation
sp specific
t total
 ν void

v volume
x,y,z Cartesian coordinates (dimensions)
 1,2,3 components

Declaration of Competing Interest

There are no conflicts of interest with coauthors (I am the sole contributor) or financial counterparts.

Data availability

The data used is own unpublished data or has been published and proper reference is given.

Acknowledgements

Academy of Finland is acknowledged for its support to Center of Excellence for Functional Materials (FunMat) at Åbo Akademi University.

References

- [1] Kitchener JA. Chem Br 1977;13:105.
- [2] Feynman RP. There's plenty of room at the bottom. California Institute of Technology, USA: Engineering and Science; 1960.
- [3] Lide DR, editor. Handbook of chemistry and physics. 87th ed. Boca Raton, Florida, USA: CRC Taylor & Francis; 2006.
- [4] Israelachvili J. Intermolecular & surface forces. 2nd ed. London, UK: Academic Press; 1992.
- [5] Hunter RJ. Foundations of colloid science. 2nd ed. Oxford, UK: Oxford University Press; 2001.
- [6] Rosenholm JB. Adv Colloid Interface Sci 2010;156:14.
- [7] Heywood H. Symp Size Anal Inst Chem Eng Suppl 1947;25:14.
- [8] Heywood H. J Pharm Pharmac Suppl 1963;15:56T.
- [9] Allen AT. Particle size measurement. 4th ed. London, UK: Chapman & Hall; 1990.
- [10] Wadell H. J Geol 1932;40:443.
- [11] Wadell H. J Geol 1933;41:310.
- [12] Sneed ED, Folk RL. J Geol 1958;66:114.
- [13] Wadell H. J Geol 1935;43:250.
- [14] Webb PA, Orr C. Analytical methods in fine particle technology. Norcross, GA, USA: Micromeritics Instrument Co; 1997.
- [15] Cumberland DJ, Crawford RJ. The packing of particles. Oxford, UK: Elsevier; 1987.
- [16] Lyklema J. Fundamentals of interface and colloid science. In: Fundamentals. vol. 1. London, UK: Academic Press; 1991.
- [17] Rosenholm JB. Adv Colloid Interface Sci 2015;220:8.
- [18] McNaught AD, Wilkinson A, editors. IUPAC compendium of chemical technology, "gold book". Oxford, UK: Blackwell Sci Publ; 1997.
- [19] Westman AER, Hugill HR. J Am Ceram Soc 1930;13:767.
- [20] Furnas C. Ind Eng Chem 1931;23:1052.
- [21] Prasad I, Santangelo C, Grason G. Phys Rev E 2017;96:052905.
- [22] Pillitteri S, Lumay G, Opsomer E, Vandewalle N. Sci Rep 2019;9:1.
- [23] McGeary RK. J Am Ceram Soc 1961;44:513.
- [24] Lee DJ. J Paint Tech 1970;42:579.
- [25] Blomqvist K, Bedö Z, Rosenholm JB. Colloid Polym Sci 1980;258:398.
- [26] Rosenholm JB, Laaksonen L. J Colloid Interface Sci 1988;121:309.
- [27] Beneati RF, Brosilow CB. AIChE J 1962;8:359.
- [28] Aaltonen M, Nordenswan E, Rosenholm JB. 2023 unpublished results.
- [29] Brown GG. Unit operations. New York, USA: J Wiley; 1966.
- [30] Bollobás B, Riordan O. Random structures and algorithms 29; 2006. p. 524.
- [31] Newman MEJ, Ziff RM. Phys Rev Lett 2000;85:4104.
- [32] Jokinen M, Györfvay E, Rosenholm JB. Colloids Surf A 1998;141:205.
- [33] Rosenholm JB. Adv Colloid Interface Sci 2009;146:31.
- [34] Achree Jr WA. Thermodynamic properties of nonelectrolyte solutions. Florida, USA: Academic Press; 1984.
- [35] Shinoda K. Principles of solution and solubility. New York, USA: Marcel Dekker Inc; 1978.